# Aerodynamic Effects and Heat Flux Augmentation of a Transpiration Cooled Hypersonic Sharp Leading Edge

Raghul Ravichandran* , Luke Doherty †, and Matthew McGilvray ‡
*Oxford Thermofluids Institute, University of Oxford, Oxford, United Kingdom, OX2 0ES*

Kyle Damm§ and Rowan Gollan¶
*The University of Queensland, Queensland 4072, Australia*

**This paper presents numerical results investigating the aerodynamic and aerothermal effects of mass injection applied to hypersonic sharp leading edges, in the context of active thermal protection systems. A numerical study was carried out using Eilmer to investigate the coupling of leading edge radius and mass injection on heat flux and drag augmentations. Radii from 1 mm to 25 mm were considered at blowing parameters from 0.0 to 1.5 on 2D planar leading edge at a fixed trajectory point. Drag was found to barely change with mass injection, whereas heat flux was found to significantly reduce at the leading edge. The leading edge heat flux distribution could be collapsed, and therefore predicted, straightforwardly. Film cooling predictive methods in literature for other mass injection scenarios were found to collapse the heat flux and concentration comfortably with empirical modifications.**

## Nomenclature

| | | |
|---|---|---|
| $B_h$ | = | Blowing parameter |
| $C$ | = | Coolant concentration parameter |
| $H$ | = | Specific enthalpy [J/kg] |
| $h_c$ | = | Slug height [m] |
| $M$ | = | Mach number |
| $P$ | = | Pressure[Pa] |
| $\dot{q}$ | = | Heat flux [W/m$^2$] |
| $R$ | = | Radius [m] |
| $Re_u$ | = | Boundary layer edge unit Reynolds number |
| $s$ | = | Surface coordinate [m] |
| $St$ | = | Stanton number |
| $T$ | = | Temperature [K] |
| $u$ | = | Velocity [m/s] |
| $w$ | = | Injector length [m] |
| $\gamma$ | = | Specific heat ratio |
| $\delta$ | = | Boundary layer height [m] |
| $\eta$ | = | Surface normal axis |
| $\mu$ | = | Dynamic viscosity [kg/ms] |
| $\rho$ | = | Density[kg/m$^3$] |
| $\tau_w$ | = | Skin friction [Pa] |
| $\xi$ | = | Surface tangential axis |

**Subscripts**

| | | |
|---|---|---|
| $c$ | = | Coolant |
| $e$ | = | Boundary layer edge |
| $FP$ | = | Flat plate |
| $LE$ | = | Leading edge |
| $T$ | = | Stagnation value |
| $w$ | = | Wall |
| 0 | = | Stagnation point |
| $\infty$ | = | Freestream |

*D.Phil. Candidate, Department of Engineering Science
†Departmental Lecturer, Department of Engineering Science
‡Associate Professor, Department of Engineering Science
§Postdoctoral Research Fellow, Centre for Hypersonics, School of Mechanical and Mining Engineering
¶Senior Lecturer, Centre for Hypersonics, School of Mechanical and Mining Engineering

# I. Introduction

Sharp leading edges are becoming an increasingly desirable feature on hypersonic vehicles to improve their aerodynamic characteristics for both re-entry [1] and sustained hypersonic flight [2, 3]. The improvements in lift-to-drag ratio of vehicles with sharp leading edges have been explored for hypersonic vehicles [4–6], where appreciable aerodynamic benefits are found for sharper cases. In these studies, cylindrically blunted leading edges with $R_{LE}$ ranging from 0.1 mm to 30 mm were explored. The reduction in leading edge radius is associated with an increase in heat flux [7], the mitigation of which is a topic of active research [8–10].

For missions and geometries where passive systems provide insufficient protection, and where aerodynamic shape stability requirements rule out ablative systems, active cooling systems are an effective means to mitigate high heat fluxes. While active cooling systems carry mass and complexity penalties, they may be employed in a targeted manner, such as, at a vehicle leading edge. Transpiration cooling is a promising active thermal protection system (TPS) candidate whereby coolant gas is injected into the hypersonic boundary layer via a porous injector on the vehicle surface. Two transpiration-cooled geometries are sketched in Figure 1. Transpiration cooling actively reduces the temperature of the local structure by means of three mechanisms:

1) Solid to coolant gas convective heat transfer as the gas passes through the porous material [11].
2) Film cooling, where the relatively cold gas reduces incoming heat flux by reducing thermal gradients at the wall. Boundary layer thickening due to injection has a similar effect [12].
3) Reduction of catalytic wall heating and oxidation protection, the latter of which may allow materials to operate at higher temperatures [13].

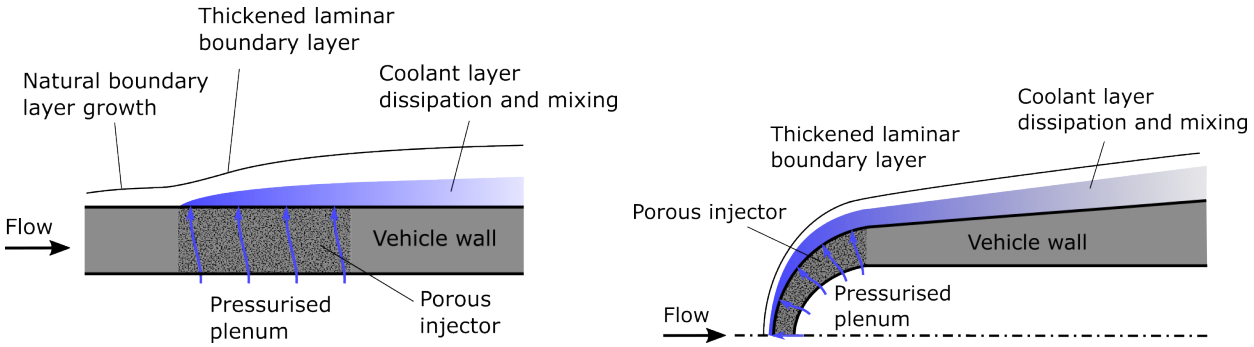


**(a) Flat plate** **(b) Leading edge**

**Figure 1: Sketches of transpiration cooling applications for hypersonic vehicles.**

Transpiration cooling has been identified as a candidate active TPS as early as the 1950s [14–17]. In the 1960s and 70s, considerable progress was made in understanding the heat flux and pressure augmentations on a variety of geometries, conditions and coolants. Such geometries include blunt body axisymmetric stagnation point injection [18–21], distributed injection around blunt bodies [22–25], and sharp cones with downstream frustum injection [26, 27]. In these studies, cases with injection at and near the stagnation point experienced significant heat flux reduction at the injector, which continued far downstream along the models. For these cases, pressure profiles remained largely the same with and without injection. On the other hand, studies where injection continued around a blunt body, or on the frustum downstream of a sharp nosetip, saw considerable downstream pressure increases. This suggests that drag penalties due to transpiration cooling may be minimised if injection is applied to the leading edge only, as shown in Figure 1b. When employing transpiration cooled sharp leading edges, there must be a compromise between the heat flux reduction, and the possible pressure drag increase due to thickening of the shock layer. It has not yet been explored whether or not these drag penalties reduce aerodynamic efficiency to that of a blunt leading edge.

More recent experimental work has focused on transpiration cooling of flat plate geometries [8, 9, 12, 13, 28–31], such as that shown in Figure 1a, with constant mass injection profiles along the injector. These studies have characterised the heat flux reduction on the porous material, film cooling effectiveness, boundary layer thickening, and coolant concentration profiles downstream of injectors.

The only recent work on leading edges with distributed outflow have used slots [32], variable permeability [33], or multiple plenums and injectors [34, 35]. These studies did not consider leading edge-only injection, and only [34] was carried out in a hypersonic facility, and took heat flux augmentation measurements. The rest were carried out in heated

subsonic facilities, or in plasma facilities [36], taking temperature measurements only.

Numerical studies have considered distributed mass fluxes on leading edges, either using a flow solver to calculate outflow distributions [32, 33, 36–38], or using a prescribed outflow [39, 40]. These numerical studies used leading edges on the order of 2-10 mm. In [41], leading edge-only mass injection was employed for small radii (0.1-3 mm) with constant mass flux. It is qualitatively shown that mass flux slightly increases the effective radius of the leading edge, and that wedge angle has no effect on leading edge or downstream cooling when transpiration cooling is limited to the leading edge only. This study did not consider drag implications or the means to correlate the heat flux distributions.

Correlations developed for axisymmetric stagnation point heat flux reduction [18, 42, 43] are useful for system studies. Similarly, correlations have been developed for film cooling of flat plate geometries [12, 31, 44]. However, there has been no further work modelling the heat flux augmentation around a sharp leading edge, including off the stagnation line.

This paper presents numerical experiments examining the interaction between the effects of mass injection and leading edge radius on cylindrically blunted leading edges, employing transpiration cooling on a leading edge injector. The integrated surface pressure and skin friction, the leading edge heat flux augmentation, and the heat flux and concentration changes downstream of the injector are all examined to understand the fundamental viability of a transpiration-cooled leading edge.

**Existing Correlations**

The blowing parameter has previously been used in heat flux reduction studies with mass injection on stagnation points [18, 42, 43]. Shown in Equation 1, $B_h$ is defined by the uncooled local Stanton number, which is proportional to $\dot{q}$. Here, $H_{aw}$ is the adiabatic wall enthalpy.

$$B_h = \frac{F}{St_0(s)} \tag{1}$$

$$F(s) = \frac{\dot{m}(s)}{\rho_\infty u_\infty} = \frac{\rho_c u_c}{\rho_\infty u_\infty} \tag{2}$$

$$St_0(s) = \frac{\dot{q}_0(s)}{\rho_\infty u_\infty (H_{aw} - H_w)} \tag{3}$$

Heat flux reduction on a stagnation point injector, has been correlated using $B_h$ in [18], and experimentally verified in [43]. This correlation is shown in Equation 4. Here, $N_f = 1$ or $5/9$ for diatomic or monatomic coolant gases respectively; $k_b$ is a shape factor equal to unity for axisymmetric stagnation points; $W$ is molecular weight; and erf is the error function.

$$\Psi = \frac{\dot{q}(0)}{\dot{q}_0(0)} = \sqrt{\pi\Lambda}\frac{\exp\{-\Lambda B_h^2\}}{1 + \mathrm{erf}\{\Lambda\}^{0.5} B_h} \tag{4a}$$

$$\Lambda = \frac{1}{\pi}\frac{\Delta}{\Delta^{uc}}\lambda^{B_h/B^*} \tag{4b}$$

$$B^* = 1.82\frac{\sqrt{\pi\epsilon(W_f/W_\infty}}{k_b(\chi'_w)^*} \tag{4c}$$

$$(\chi'_w)^* = \frac{1.187\sqrt{(8\epsilon(1-\epsilon)}}{(1+\sqrt{8/3\epsilon}) - \epsilon)(1 + 0.225\sqrt{\epsilon})} \tag{4d}$$

$$\lambda = \sqrt{\frac{W_\infty}{W_f}} N_f \tag{4e}$$

$$\frac{\Delta}{\Delta_0} = 1 + k_b\sqrt{\frac{1}{\epsilon}\frac{W_\infty}{W_f}} F \tag{4f}$$

$$\epsilon = \frac{\rho_\infty}{\rho_1} \tag{4g}$$

$$\tag{4h}$$

Film cooling correlations for flat plate geometries for thermal effectiveness and coolant concentration effectiveness have also been explored, and are presented below. The thermal effectiveness, $\eta_{th}$, is defined below in Equation 5.

$$\eta_{th} = 1 - \frac{\dot{q}}{\dot{q}_0} \tag{5}$$

To model the downstream thermal effectiveness, a film cooling correlation parameter is constructed in [45], used in [44, 46, 47], and is presented in Equation 6. Here, $\zeta_{th,FP}$ is the flat plate correlation parameter; and $C^*$ is the Chapman-Rubesin factor, where $C^* = (\rho^*\mu^*/\rho_e\mu_e)^{0.5}$, evaluated at the Eckert reference conditions [48]. In the case of slot injection in [45], $x_0$ is the distance from the leading edge to the slot, and $x_{\text{ref}}$ is a reference length to account for an incoming boundary layer thickness. In [45], $x_{\text{ref}}$ is empirically deduced to be $x_{\text{ref}} = x_0^{1.16}$ for that geometry. This geometery is shown in Figure 2.

$$\zeta_{th,FP} = \frac{1}{Fw}\sqrt{\frac{x - x_0}{x_{\text{ref}}}\frac{C^* x}{Re_u}} \tag{6}$$

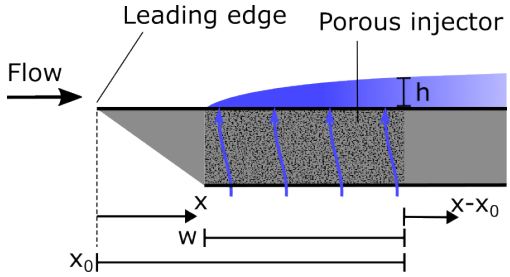


**Figure 2: Film cooling correlation reference coordinates and dimensions.**

Correlations in [44, 46, 47] have used the correlation parameter to express thermal effectiveness for these flat plate geometries, a general form of which is given in Equation 7. The coefficients $\alpha$, $\beta$ and $\gamma$ are empirically found using numerical or experimental data. For the flat plate data in [44], the coefficients $\alpha = 0.4$, $\beta = 0.96$, and $\gamma = -1$.

$$\eta_{th,FP} = \begin{cases} 1 & \text{for } \xi \leq \beta \\ [1 + \alpha(\zeta_{c,FP} - \beta)]^{\gamma} & \text{for } \xi > \beta \end{cases} \tag{7}$$

Similar to the thermal efficiency, a concentration efficiency, $\eta_c$ can be used as a measure of the coolant concentration distribution at the wall. This is defined below in Equation 8, where $C$ is a concentration parameter, defined below using mole fraction, $X$.

$$\eta_c = C(s, y = 0) \tag{8}$$

$$C(s, y) = \frac{X_c - X_{c,\infty}}{1 - X_{c,\infty}} \tag{9}$$

A correlation parameter, $\zeta_{c,FP}$, is defined in [49] for the coolant concentration downstream of a flat plate injector, and is shown in Equation 10.

$$\zeta_{c,FP} = \sqrt{\frac{u_e h^2}{4D(x - x_0)}} \tag{10}$$

This was developed by considering the diffusion-advection problem of a coolant gas slug injected into the boundary layer. The solution of this problem is shown in Equation 11.

$$\eta_{c,FP} = \eta_{c,FP}(x_0)\,(\text{erf}\{\zeta\}) \tag{11}$$

Here, $D_{12}$ is the binary diffusion coefficient, estimated using the Lennard-Jones diffusion parameters which may be found in [50]; and $u_e$ is the boundary layer edge velocity. The coordinates are consistent with Figure 2. $h$ is the coolant gas slug height at the end of the injector, approximated in [49] using a control volume around the injector. An empirical definition was also derived, shown in Equation 12, where $C_0 = C(x_0, 0)$.

$$h = \begin{cases} y(C = 0.99C_0) & \text{for } C_0 = 1 \\ y(C = 0.95C_0) & \text{for } C_0 < 1 \end{cases} \tag{12}$$

## II. Simluation Setup

The solver used in this study is the open-source multi-physics flow solver, Eilmer [51], part of the GDTk [52] gas dynamics toolkit developed at the University of Queensland. Eilmer is a general-purpose hypersonic simulation program that can solve the Euler, Navier-Stokes or Reynolds-Averaged Navier-Stokes equations on either structured or unstructured, two- or three-dimensional body-fitted grids using explicit time integration or Newton-Krylov acceleration for steady-state problems. For this work, Eilmer is used to solve the Navier-Stokes flow equations for a multi-species reacting gas in thermodynamic equilibrium on a two-dimensional grid of structured quadrilateral elements. This section will briefly outline the boundary conditions, simulation settings and the numerical methods employed in this study. A more complete description of the Eilmer solver may be found in [51, 53–55].

### A. Test Conditions and Geometry

The freestream conditions were kept fixed, and the leading edge geometry was defined to generate comparable cases for integrated aerodynamic properties. The trajectory point of $M_\infty$ = 7 and altitude = 35 km was chosen, as these conditions are relevant for both the ascent and descent of a spaceplane. Freestream conditions are listed in Table 1. Nitrogen coolant was used for mass injection along the leading edge only. Defined in [18], the boundary layer blowoff parameter was used to limit mass injection to ensure that the boundary layer remained laminar and attached. The blowoff parameter, $B^*$ in Equation 4, is dependent on freestream conditions only, and was calculated to be $B^*$ = 1.67 for the trajectory point.

The test matrix was devised by considering the blowing parameter limit and the range of leading edge radii considered in Section I. As such, radii of $R_{LE}$ = 1, 5, 10, 25 mm were tested against blowing parameters of $B_h$ = 0.0, 0.5, 1.0, 1.5. The leading edge geometry parameters are included in Table 1, and sketched in Figure 3.

**Table 1 List of conditions and geometric parameters**

| $M_\infty$ | Alt. (km) | $u_\infty$ (m/s) | $P_\infty$ (Pa) | $T_\infty$ (K) | $T_w$ (K) | $B_{h,max}$ | Coolant | $\theta_w$ ($^o$) | $L_{BASE}$ (mm) | Geometry type |
|---|---|---|---|---|---|---|---|---|---|---|
| 7 | 35 | 2163 | 567.2 | 236.8 | 300 | 1.67 | $N_2$ | 5 | 400 | Planar 2D |

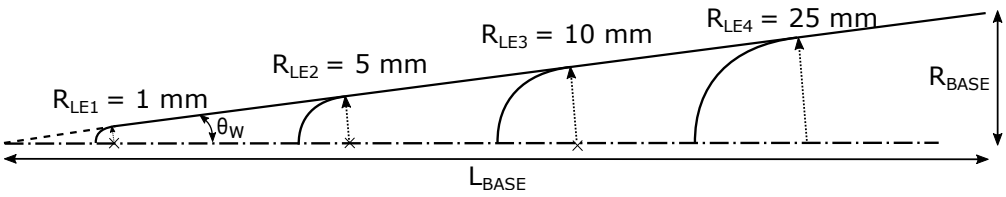


**Figure 3: Definition of leading edge geometry with variable bluntness.**

### B. Solver Settings

The key settings of the simulation are listed in 2, and discussed further below.

**Table 2 Solver settings used in numerical work**

| Flow characteristic | Assumption |
|---|---|
| Mass injection distribution | Constant blowing parameter |
| Timestepping | Steady state |
| Turbulence model | Laminar |
| Wall temperature | Cold wall, 300K |
| Chemical reactions | Chemically reacting, 1 temperature (5 species, air) |

*Mass injection distribution*

It is more meaningful to apply high rates of transpiration cooling to regions of high heat flux. In the case of a leading edge, a higher mass flux is required around a smaller $R_{LE}$ than a larger one. Additionally, heat flux tapers off quickly around the curvature of the leading edge [56], and so coolant mass flux should taper around the surface.It is therefore of interest to try to find a meaningful parameter to adequately adjust the local mass flux in such a way to provide reproducible local heat flux reduction.

To help understand heat flux augmentation over the mass injector, a mass injection distribution following a constant blowing parameter was used. Using the uncooled simulation results and Equation 1, the required mass flux distributions, $\dot{m}(s)$ are calculated for each $R_{LE}$ and $B_h$ and select cases are shown in Figure 4. It can be seen that the result of of using a constant $B_h$ is a mass flux that is scaled down with increasing $R_{LE}$, and is tapered around the surface. The mass flux distributions are proportional to $\dot{q}$ and are therefore the same shape.

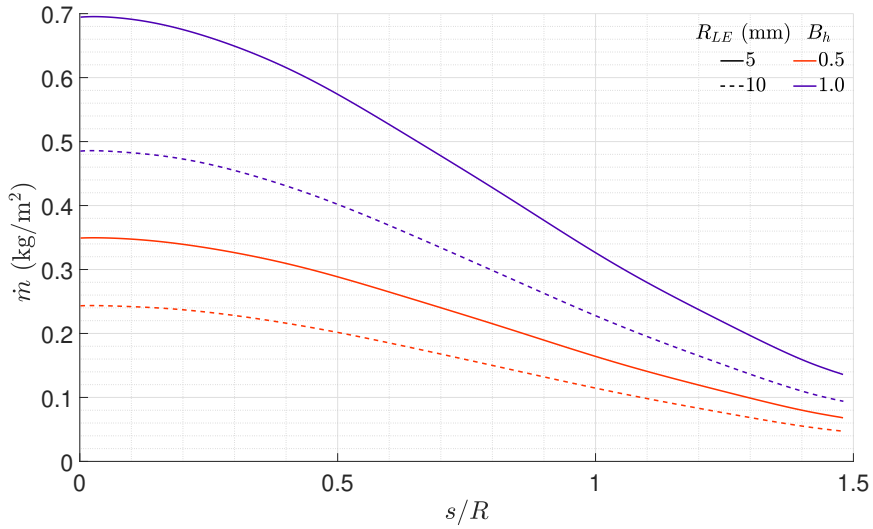


**Figure 4: Implemented mass flux along the leading edge.**

*Laminar solver*

The promotion of turbulence due to mass injection has been studied for flat plates geometries [57], where transition may be promoted if $F > 0.04$. Turbulence in the boundary layer encourages mixing of the hot post-shock gas with the coolant, nullifying and possibly increasing heat flux downstream of the injector. Transition onset for the transpiration cooling of cylindrically or spherically blunted bodies is an area of active research. Recent preliminary studies have showed that that mass injection on an axisymmetric nosetip may delay transition with moderate mass fluxes and light gases [34].

For the purposes of this study, the promotion of turbulence is considered to be delineated by a maximum blowing parameter $B^*$, considered above, and discussed in [18]. By ensuring $B_h < B^*$, the flow solver was set to solve laminar flows.

### C. Boundary Conditions

A list of boundary conditions and a corresponding sketch are shown in Table 3 and Figure 5 respectively. The profile of the inflow boundary, BC1, is obtained through an initial inviscid shock-fitting phase, to ensure appropriate grid alignment for the steady-state accelerator. Implementation of the mass flux boundary condition, BC3, is detailed in [58], where coolant velocity and concentration at the wall are calculated for each cell during each solver step using the mass and species continuity equations, respectively.

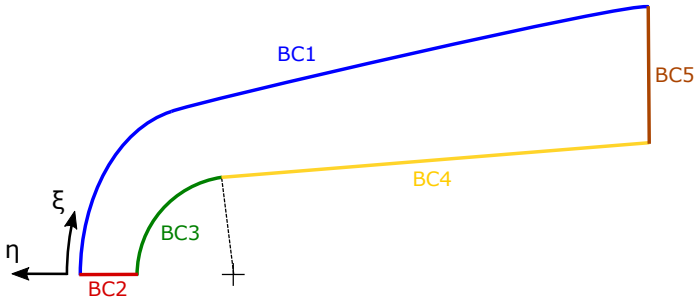


**Figure 5: Sketch of the domain shape and boundary conditions used with the steady state solver.**

**Table 3 List of boundary conditions corresponding to Figure 5**

| | |
|---|---|
| BC1 | Supersonic inflow; shock-fitted |
| BC2 | Symmetry |
| BC3 | Mass injection, no-slip wall |
| BC4 | Constant temperature, no-slip wall |
| BC5 | Supersonic outflow |

### D. Governing Equations

The flow in this study is modelled using the compressible Navier-Stokes equations, which assume continuum flow and Newtonian behaviour of the fluid. The Navier-Stokes equations in their integral form are written as follows,

$$\frac{\partial}{\partial t}\int_V \boldsymbol{U} dV = -\oint_S (\boldsymbol{F_c} - \boldsymbol{F_v}) \cdot \hat{\boldsymbol{n}} dA + \int_V \boldsymbol{Q} dV, \tag{13}$$

where $\boldsymbol{U}$ is the vector of conserved variables (mass, momentum, energy), $t$ is time, $V$ is volume, $dA$ is area, $\boldsymbol{F_c}$ is the convective flux vector, $\boldsymbol{F_v}$ is the viscous flux vector, and $\boldsymbol{Q}$ is the source term vector. For the calculations presented in this work, a thermally perfect 5-species air model ($N_2$, $O_2$, $NO$, $N$, $O$) is used. The reaction scheme of Gutpa et al. [59] is employed to compute the rate coefficients, and the chemical source term arising in equation 13 is computed using a finite-rate chemistry model. In Eilmer, each species has a curve-fit for its thermodynamic and transport properties taken from the NASA Glenn thermodynamic database [60]. The mixture thermodynamic state variables are evaluated as a simple mass fraction weighted sum of the corresponding individual species values. The calculation of mixture transport properties (e.g. such as viscosity $\mu$, thermal conductivity $\kappa$, and species diffusion $D_s$) requires a mixing rule. A variant of Wilke's mixing rule [61] is employed, specifically the mixing rules used by Gordon and McBride [62] are used to evaluate the mixture transport properties in Eilmer.

### E. Spatial Discretisation

Eilmer employs a cell-centered finite volume method to discretise Equation 13. This gives the semi-discrete form of the governing equations,

$$\frac{\partial \boldsymbol{U}}{\partial t} = -\frac{1}{V}\sum_{faces} (\mathbf{F}_c - \mathbf{F}_v) \cdot \hat{\mathbf{n}}\, dA + \mathbf{Q}, \tag{14}$$

where $\boldsymbol{U}$ and $\boldsymbol{Q}$ now represent cell-average values, $dA$ is a face area, and $\sum_{faces}$ denotes summation over the cell faces. In this work, the convective fluxes ($\boldsymbol{F}_c$) are computed using an adaptive calculator that selects the AUSMDV scheme by Wada and Liou [63] away from shocks and Hänel's method [64] near shocks. The switching between the two flux calculators is governed by a shock detector that is a simple measure of the relative change in normal velocity at interfaces. Second-order spatial accuracy for the convective fluxes is achieved by reconstructing the primitive flow state variables within the finite-volumes using a piecewise-parabolic scheme. To ensure stability when reconstructing the flow state in finite-volumes near shocks, the limiter by van Albada et al. [65] is employed. In regions with very strong gradients, further dissipation is added by multiplying the standard limiter value by the heuristic pressure-based limiter value outlined in the work by Drayna [66]. The spatial gradients for computing the viscous fluxes ($\mathbf{F}_v$) are computed using a cell-centered weighted least-squares method and the face-tangent augmented face-gradient method [67].

### F. Steady-State Accelerator

This work is interested in the steady-state solutions to the governing equations. A fully-implicit scheme is favourable for solving such problems. To derive the update scheme, the right-hand side terms in equation 14 are collected in into a vector a residual:

$$\frac{\partial \mathbf{U}}{\partial t} = \mathbf{R}(\mathbf{U}). \tag{15}$$

Using a backward difference to discretise the time derivative, recovers the fully discrete form of the governing equations as follows,

$$\frac{\Delta \mathbf{U}^k}{\Delta t} = \mathbf{R}(\mathbf{U}^{k+1}).$$

This is implicit since $\boldsymbol{U}^{k+1}$ are unknowns, and is approximated using the known state $\boldsymbol{U}^k$ and a first order linearisation of the residual vector,

$$\frac{\Delta \mathbf{U}^k}{\Delta t} = \mathbf{R}(\mathbf{U}^k) + \frac{\partial \mathbf{R}(\mathbf{U}^k)}{\partial \mathbf{U}^k} \Delta \mathbf{U}^k. \tag{16}$$

This can then be rearranged to recover the implicit-Euler time marching iterate,

$$\left[ \frac{1}{\Delta t} \mathbf{I} - \frac{\partial \mathbf{R}(\mathbf{U}^k)}{\partial \mathbf{U}^k} \right] \Delta \mathbf{U}^k = \mathbf{R}(\mathbf{U}^k), \quad \mathbf{U}^{k+1} = \mathbf{U}^k + \Delta \mathbf{U}^k. \tag{17}$$

A globalised Newton-Krylov method is used to accelerate convergence to the steady-state solution [68]. Specifically, Newton's method is used to solve for $\boldsymbol{R}(\boldsymbol{U}) = 0$, where the linear system of equations arising at each nonlinear step (i.e. equation 17) is solved iteratively via a preconditioned GMRES method [69]. Noting that as the pseudo-transient term $1/\Delta t$ approaches 0 in equation 17 (i.e. for very large $\Delta t$), Newton's method is recovered. Robust preconditioning is achieved by an incomplete LU factorization of an approximate flow Jacobian constructed by only considering a nearest-face-neighbour stencil. To reduce the computational cost of constructing the preconditioner matrix, the Jacobian is frozen for a user-selectable number of iterations.

### G. Grid Convergence

To nullify the effects of mesh-dependency on the results, a grid convergence study was carried out for each domain size. The grid convergence study was carried out using the boundary conditions above, using the steady-state accelerator described above. Each grid was created using Eilmer's in-built grid generation, where cell numbers and growth rates for both the radial and tangential directions were variables to be considered. Since heat flux modelling is of particular importance in this study, heat flux was used as the main variable for assessing the level of convergence.

Radial ($\eta$) and tangential ($\xi$) directions with respect to the grid are shown in Figure 6. The mesh parameters for the study are the cell numbers ($n_\eta$ and $n_\xi$), and the cell growth rates ($\beta_\xi$ and $\beta_\eta$). For the grid convergence study, these grid parameters were systematically varied. Initial grid sizing was found by considering the following initial constraints:

- The target wall cell thickness was kept at 1 $\mu$m
- The wall Reynolds number was kept below 1
- The $y^+$ value at the wall was kept below 1
- Cell clustering in the $\eta$ direction was symmetrically applied toward the body surface and the shock boundary (BCs 1,3,4),
- Mild cell clustering was applied in the $\xi$ direction toward the stagnation point, such that The cell growth rate from the stagnation point was 1.3.

Each grid was run to either achieve a global residual $\boldsymbol{R}(\boldsymbol{U}) = 0 < 1e-13$, or a maximum of 300k steps. Since mass injection barely changes the domain shape (see Section III), the domain size is chiefly characterised by $R_{LE}$. Therefore, each radius-based domain was tested at $B_h = 1.5$, and the same grid parameters were applied to all $B_h$ values.
The grid convergence parameters for $R_{LE} = 1$ mm are shown in Table 4, and the heat flux distribution results are shown in Figure 7. The same procedures were carried out for the other geometries, and are not shown here for brevity. The final grid parameters for all geometries are shown in Table 5.

**Table 4 Grid parameters used in the grid convergence study for $R_{LE}$ = 1 mm.**

| Grid Number | $n_\eta$ | $n_\xi$ | $\beta_\eta$ |
|---|---|---|---|
| 1 | 100 | 200 | 1.005 |
| 2 | 200 | 300 | 1.01 |
| 3 | 400 | 450 | 1.05 |
| 4 | 800 | 675 | 1.01 |

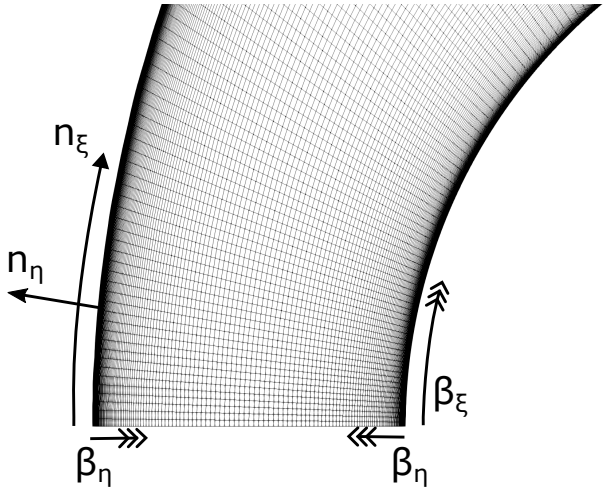


**Figure 6: Cell clustering and directions for grid parameters considered in the grid convergence study. Grid zoomed into stagnation point.**

Using the results of absolute heat flux for the four grids in Figure 7, it is clear that mesh dependency is highest at regions with the highest gradients, near the stagnation point. For this reason, it is useful to zoom into the leading edge region. Here it can be seen that while Grid 2 fails to accurately resolve the stagnation point heat flux, the difference between Grids 3 and 4 are very small (< 0.1%) along the leading edge and the rest of the domain. As such, Grid 3 was selected for the 1 mm cases. Following a similar process for the other domain sizes, the grid parameters shown in Table 4 were used to conduct the simulations for this study.

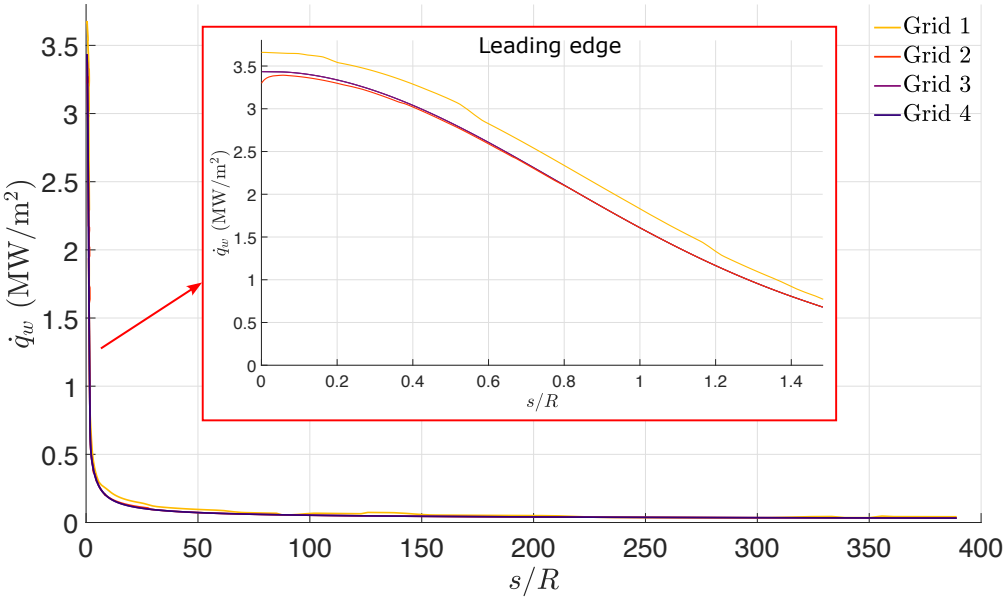


**Figure 7: Heat flux convergence for $R_{LE}$ = 1 mm, $B_h$ = 1.5.**

**Table 5 Finalised grid parameters used in the remainder of this study, following grid convergence.**

| Grid | $n_\eta$ | $n_\xi$ | $\beta_\eta$ |
|---|---|---|---|
| 1 | 400 | 450 | 1.01 |
| 2 | 450 | 450 | 1.01 |
| 3 | 550 | 350 | 1.05 |
| 4 | 600 | 300 | 1.05 |

## III. Results

The purpose of the current study is to understand how leading edge mass injection affects the flowfield, and how these effects are influenced by the change in mass flux and radius. Plots of flowfield contours and surface pressures and heat fluxes for $R_{LE}$ = 5 mm, $B_h$ = 1 are first explored for overall context and are representative of the entire dataset. Figure 8 shows the contour plot of temperature and pressure for the whole domain of this specific case. Figure 9 plots the static and total enthalpy when zoomed in on the leading edge, showing the high gradients at the leading edge which quickly fall off downstream. Figure 10 plots the temperature and nitrogen coolant concentration zoomed in at the stagnation region. Here, the approximate location of the dividing streamline can be shown to add a small artificial thickness to the leading edge.

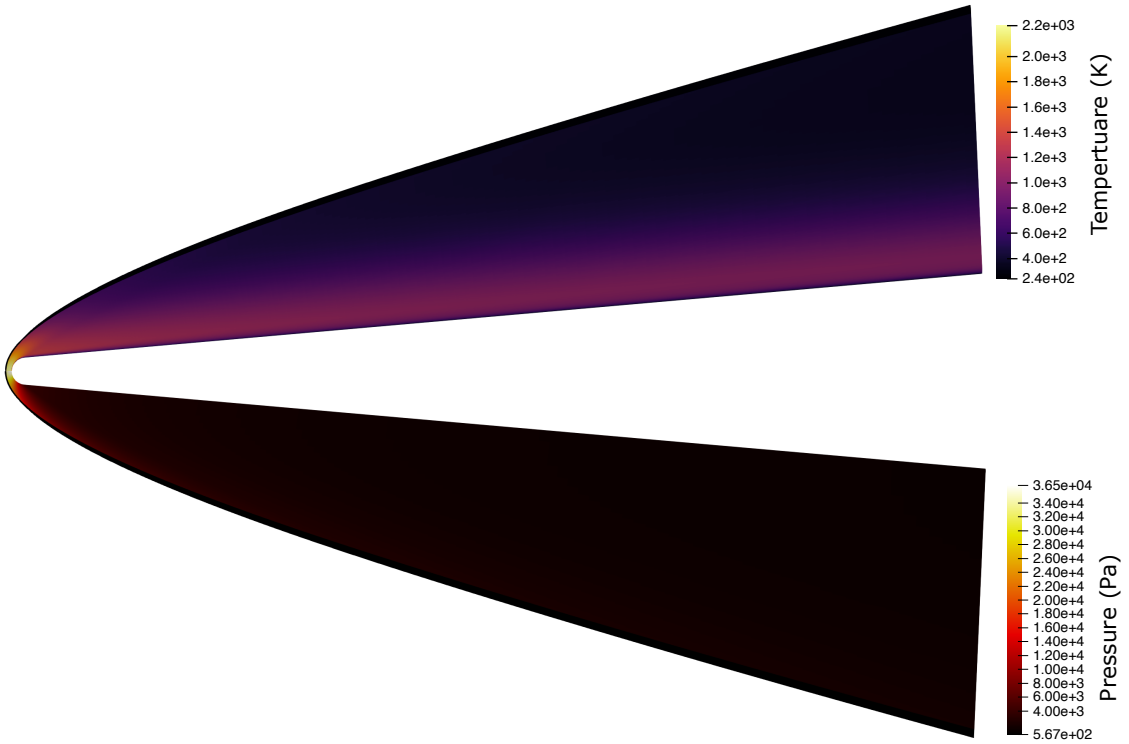


**Figure 8: Contour plot of the temperature and pressure fields throughout the domain for $R_{LE}$ = 5 mm, $B_h$ = 1.**

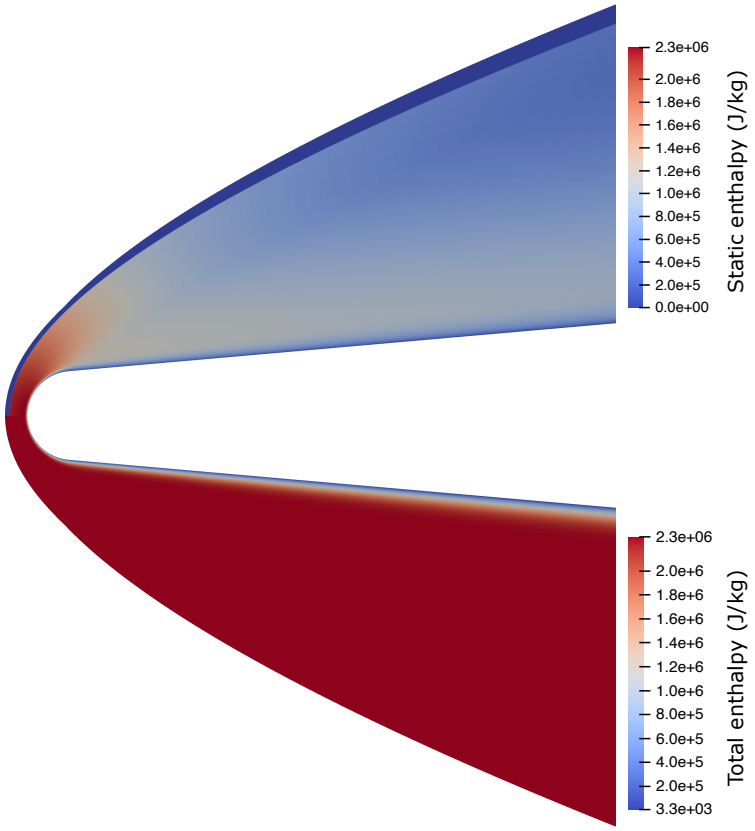


**Figure 9: Contour plot of the total and static enthalpy fields zoomed in toward the leading edge for $R_{LE}$ = 5 mm, $B_h$ = 1.**

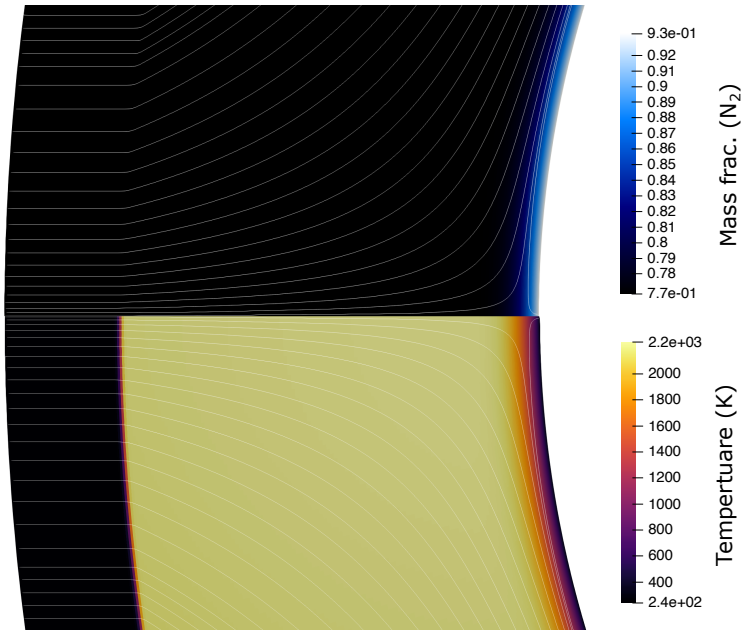


**Figure 10: Contour plot of the flowfield, zoomed in to the stagnation region. $N_2$ concentration (top) and temperature (bottom) fields with streamlines for $R_{LE}$ = 5mm, $B_h$ = 1 case.**

Particular focuses of this paper include the drag and heat flux augmentations; the change in shock structure due to mass injection; and the coolant dissipation downstream of the injector alongside the heat flux reduction. Absolute surface heat flux and pressure for the $R_{LE}$ = 5mm case with $B_h$ = 0 & 1 are shown below in Figure 11.

In the results section of the paper, drag results are presented along the leading edge injector and then integrated over the body as a whole. Heat flux results are presented according to three separate regions of interest: the stagnation point, the leading edge injector, and the wedge downstream of the injector. Due to the truncation of the downstream domain for the larger $R_{LE}$ cases (see Figure 3), the downstream heat flux and concentration analysis is carried out for the $R_{LE}$ = 1,5 mm cases.

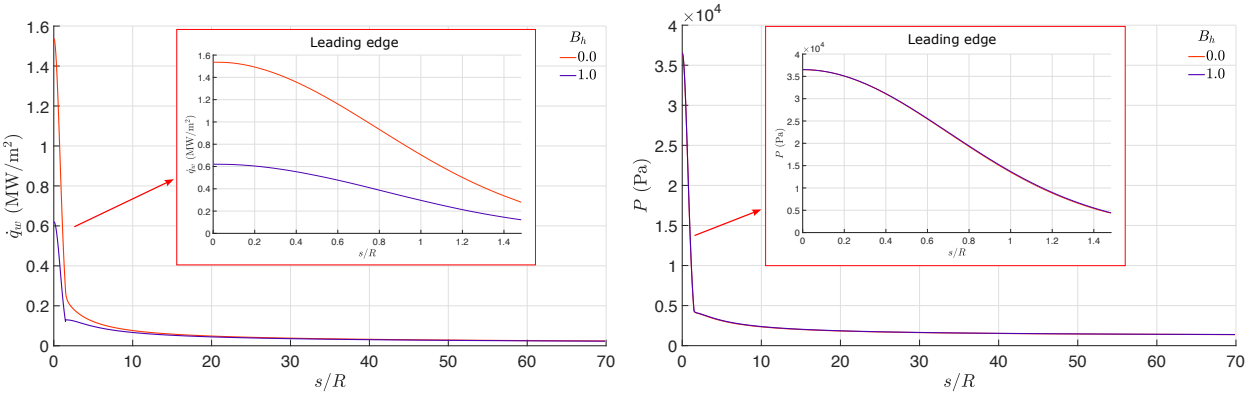


**(a) Absolute heat flux.** **(b) Absolute pressure.**

**Figure 11: Plots of surface quantities for $R_{LE}$ = 5mm case with $B_h$ = 0 & 1.**

### A. Shock layer and boundary layer thickness

Understanding how the shock and boundary layers thicken due to coolant injection are a first step in understanding the drag and heat flux augmentations. Using the detection methods described further below, the shock and boundary layer shapes over the body are shown for the $R_{LE}$ = 5 mm case in Figure 12.

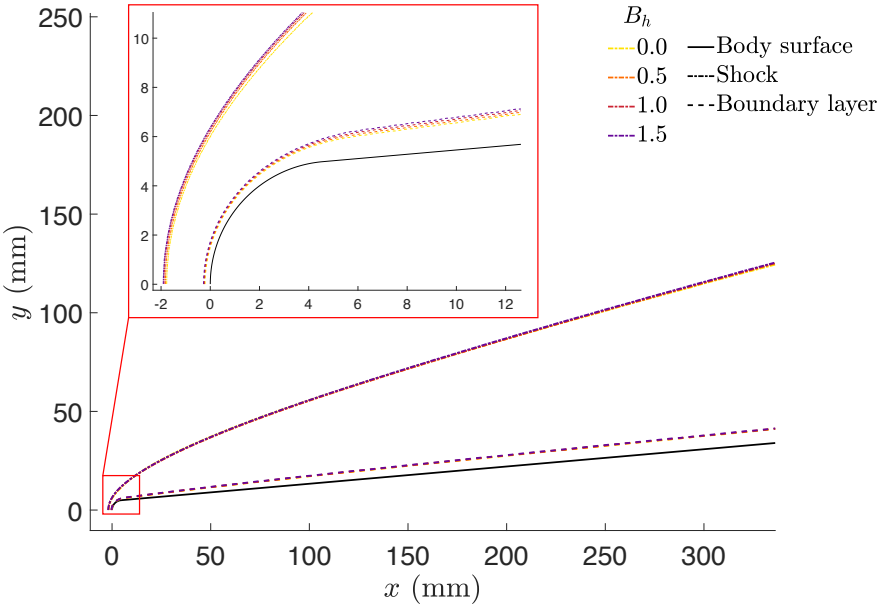


**Figure 12: Shock and boundary layer shape over the body for $R_{LE}$ = 5 mm.**

From this, the change in the shock standoff distance, shock angle and boundary layer thickness are of interest. These

are shown in Figures 13, 14, and 15 for the $R_{LE} = 5$ mm case.

The location of the shock was determined using Eilmer's in-built shock detector, described in Section II. Figure 13 plots the relative shock layer thickening due to mass injection, $\Delta_{sh}/\Delta_{sh,0}$, along with the absolute shock layer thickness. The shock layer thickening persists far downstream, and is quite small, settling below a 5% difference to the uncooled case. The shock angle was measured relative to the freestream, shown in Figure 14. The change in shock angle barely exceeds 3%, and in the downstream regions, $B_h$ does not seem make much difference to shock angle. These results suggest, that mass injection seems to slightly increase the effective bluntness of the leading edge, but barely affects the dowsntream wedge angle seen by the inviscid flow.

The enthalpy-based boundary layer location is described by Equation 18. A plot of the absolute and relative boundary layer thickness is shown in Figure 15. The figure suggests a similar to that of the shock: the amount of boundary layer thickening is dependent on $B_h$ and the effect persists far downstream of the injector. Boundary layer thickening leads to reduced velocity and temperature gradients at the wall, which in turn leads to sustained skin friction and heat flux reduction, as discussed in [45].

$$H(\delta) = 0.99(H_{T,\infty} - H_w) \tag{18}$$

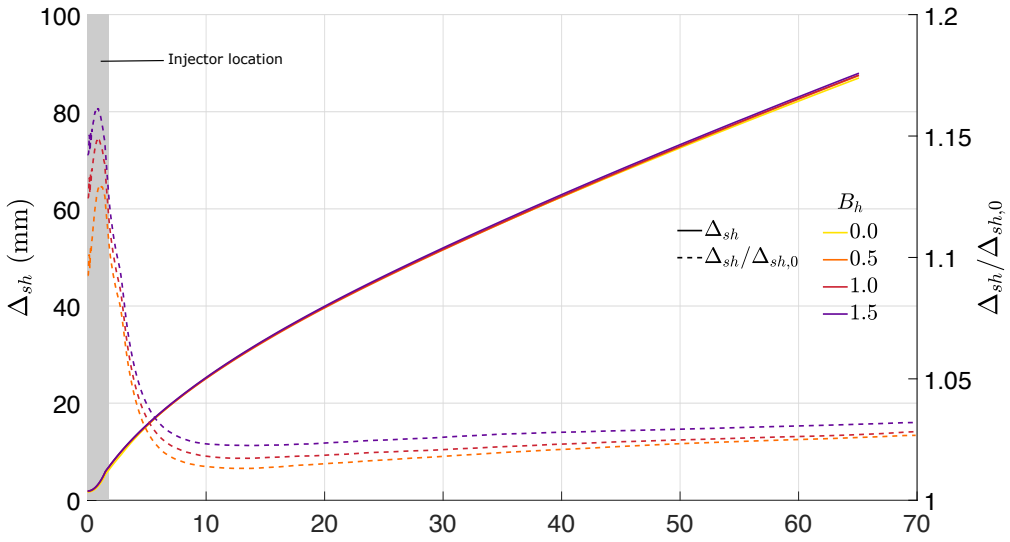


**Figure 13: Shock layer thickness distributions for $R_{LE} = 5$ mm.**

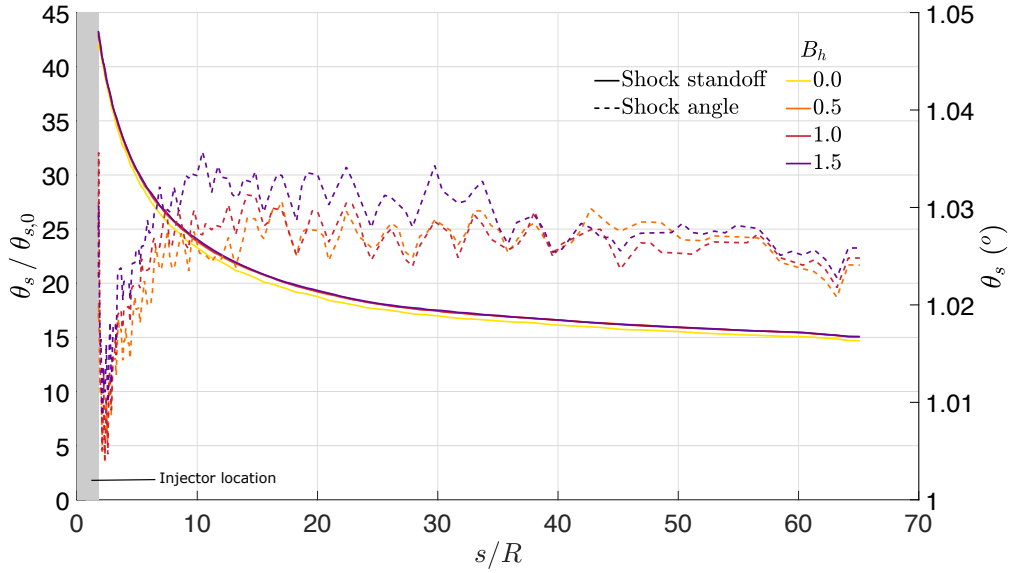


**Figure 14: Shock angle distributions for $R_{LE}$ = 5 mm.**

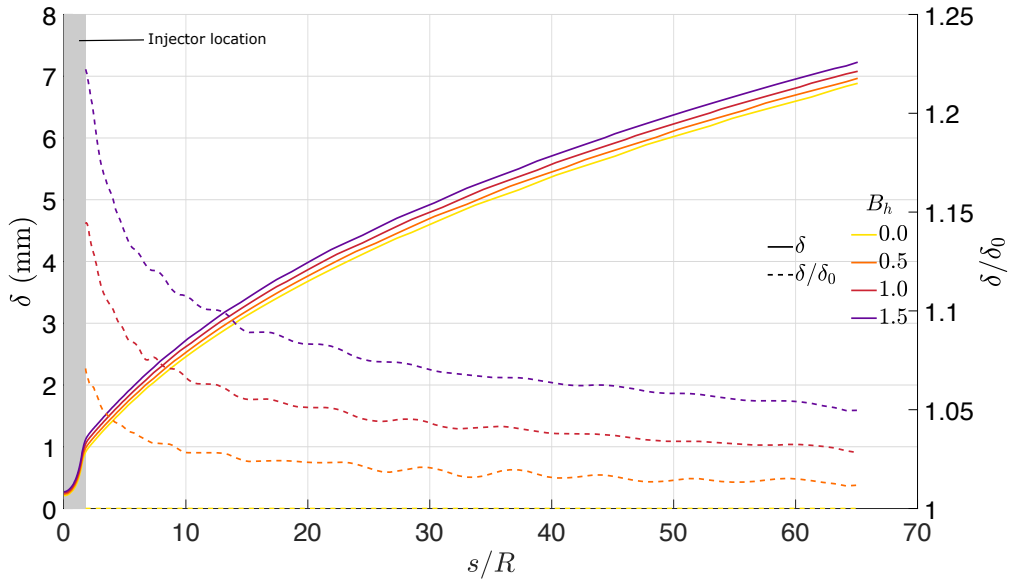


**Figure 15: Boundary layer thickness distributions for $R_{LE}$ = 5 mm.**

### B. Drag

Plots of pressure and skin friction for all cases are presented in Figure 29 in the Appendix, with the specific case of $R_{LE}$ = 5 mm shown below in Figure 16. Distributions along the whole body are in the main axes, and are zoomed in on the leading edge injector in the inset plots. These force distributions are then resolved in the axial direction and integrated over the surface to obtain the body drag, and are shown in Figure 17.

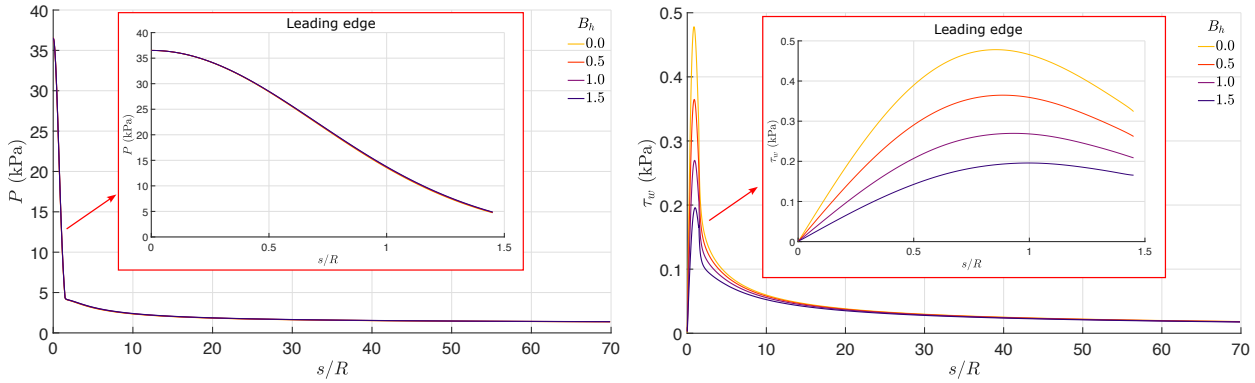


**(a) Pressure** **(b) Skin friction**

**Figure 16: Force distributions acting on the $R_{LE}$ = 5 mm body, with inset plots showing leading edge distributions.**

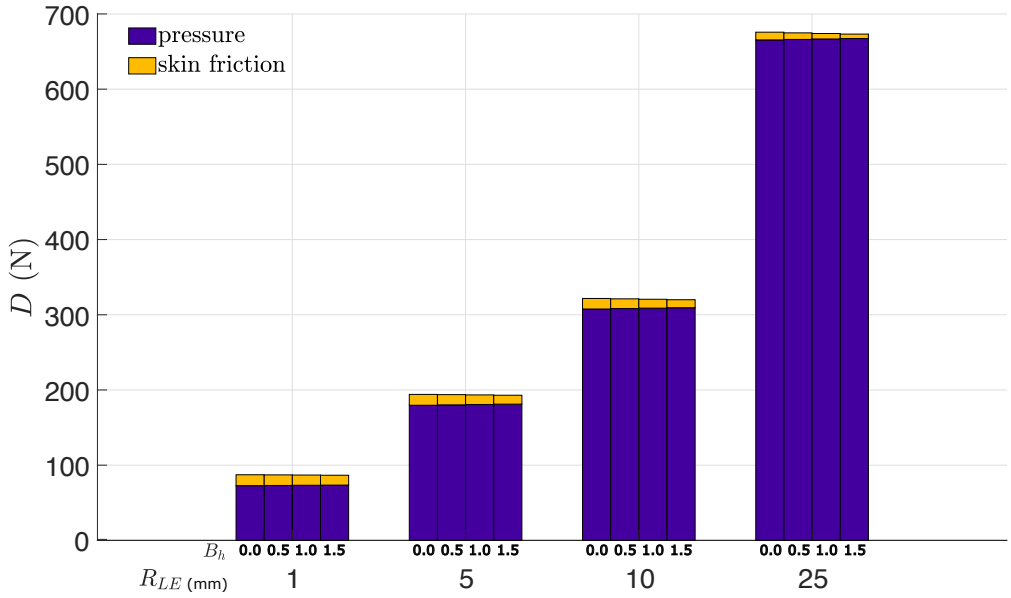


**Figure 17: Integrated drag of each mass injection and radius.**

Overall, changes in drag are dominated by the change in radius, increasing by 2.2 times for the change in $R_{LE}$ from 1 mm to 5 mm, and by 7.7 times for the change up to $R_{LE}$ = 25 mm. While these results are specific to the geometries and conditions selected, the trends provide useful information in understanding the relative magnitude changes in the drag.

These results show that pressure drag dominates for these geometries, accounting for around 83.4% of total drag for $R_{LE}$ = 1 mm, and 98.5% for $R_{LE}$ = 25 mm. Both distributed and integrated plots show that pressure augmentation due to mass injection is very small, which follows on from small changes in shock layer properties noted above. The pressure drag increase between the maximum and no injection cases is 1.5% for $R_{LE}$ = 1 mm, and 0.6% for $R_{LE}$ = 25 mm. Peak skin friction and integrated skin friction drag are higher for sharper leading edges, however mass injection actually reduces the skin friction over the leading edge.

### C. Leading edge heat flux

*Uncooled Leading Edge*

The Fay-Riddell correlation, shown in Equation 19 can be used to calculate the uncooled convective stagnation point heat flux. A $\sqrt{3}$ factor is included to account for the change in heat flux associated with a change in geometry from

axisymmetric to planar [70].

The uncooled convective heat flux distribution around the leading edge may be calculated using Lees' heat flux distribution [56], shown in Equation 20, where along the leading edge $\theta \leq \frac{\pi}{2} - \alpha_{\text{wedge}}$. Here, $\alpha_{\text{wedge}}$ is the wedge angle and $\theta$ is the surface subtended angle from the stagnation point. The distribution is limited such that $\dot{q}(\theta = 0) = \dot{q}_0$.

$$\dot{q}_0(0) = \frac{0.763}{Pr_w^{0.6}} (\rho_e \mu_e)^{0.4} (\rho_w \mu_w)^{0.1} (H_{0e} - H_w) \left[1 + \left(Le^{0.52} - 1\right) \frac{H_d}{H_{0e}}\right] \left(\frac{du_e}{dx}\right)^{0.5} \frac{1}{\sqrt{3}} \tag{19}$$

$$\dot{q}_0(s) = \dot{q}_0(0) \cdot D^{-0.5} \left[2\theta \sin(\theta)[(1 - K_\infty)\cos^2(\theta) + K_\infty\right] \tag{20a}$$

$$D = (1 - K_\infty)\left(\theta^2 - \frac{\theta \sin(4\theta)}{2} + \frac{1 - \cos(4\theta)}{8}\right) + 4K_\infty \left(\theta^2 - \theta \sin(2\theta) + \frac{1 - \cos(2\theta)}{2}\right) \tag{20b}$$

$$K_\infty = \frac{1}{\gamma_\infty M_\infty^2} \tag{20c}$$

$$\tag{20d}$$

Equations 19 and 20 can be used to obtain the uncooled heat flux distribution along the leading edge. This is plotted in Figure 18, along with the uncooled numerical results for the different radii. There is reasonable agreement at the stagnation point, and a slight deviation in heat flux profile over the curved surface.

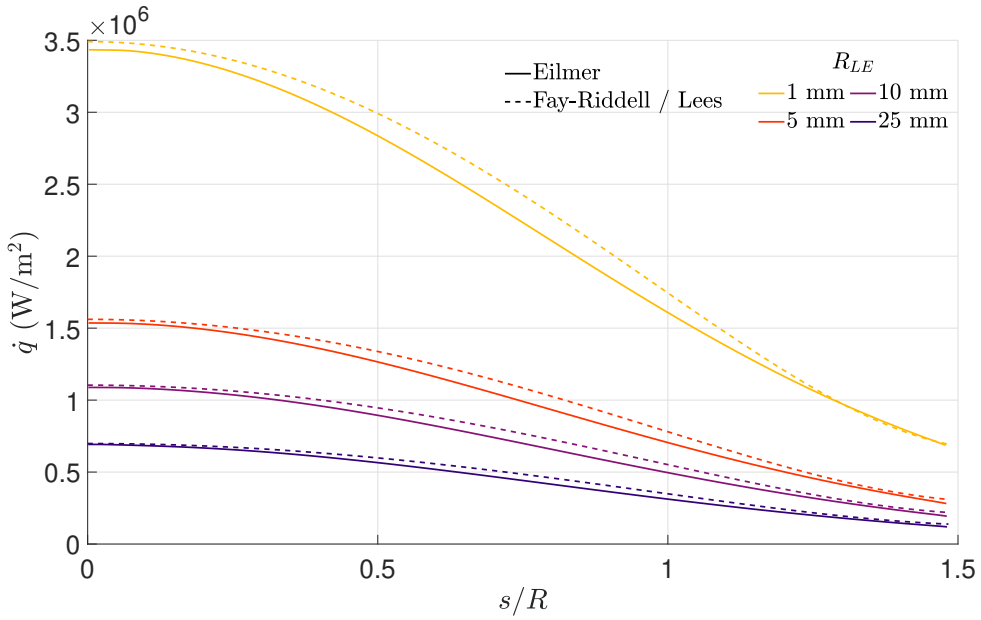


**Figure 18: Comparison of theoretical and numerical uncooled heat flux distribution along the leading edge.**

*Cooled Leading Edge*

The numerical results for the stagnation point heat flux reduction is compared against the semi-analytic heat flux reduction in Equation 4. These results are plotted in Figure 19, and show reasonable agreement. Previously mentioned, in Equation 4, $k_b = 1$ for an axisymmetric stagnation point [18]. Although the results in the figure show reasonable agreement, further work may be needed to derive $k_B$ for a planar stagnation point across a wide range of conditions.

It is worth noting that in plotting Equation 4, a fixed $B_h$ does not entirely collapse $\Psi$ for different $R_{LE}$. While most components of Equation 4 are $B_h$ dependent, the shock standoff augmentation, $\frac{\Delta}{\Delta_0}$ is a mass flux balance dependent on $F$ (which itself is dependent on $St_0$ and therefore $R_{LE}$).

Since the flow over the leading edge is still directly over a porous injector, the cooled stagnation point heat flux, $\dot{q}(0)$, is used as a parameter to collapse the rest of the cooled heat flux distribution, $\dot{q}(s)$. Shown in Figure 20, the distributions collapse quite well.

It is thought that the minor variations in the normalised heat flux distributions are due to non-linear secondary effects, caused by changing $R_{LE}$ and $B_h$. A constant $B_h$ for different $R_{LE}$ changes the mass flux, leading to a non-linear scaling of $\Delta_{sh}/\Delta_{sh,0}$ with $B_h$. This change in the shock layer may affect the the heat flux, especially since temperature gradients are sensitive to the very thin shock layer in this region. It is also considered that the physical size of the different geometries are not accounted for in the normalisation. Considering that the length-based Reynolds number, $Re_s$, changes between radii, and that for flat plate boundary layer theory [48], $\dot{q}_0 \propto \sqrt{Re_s}$, the difference in $Re_s$ along the surface may contribute toward the variations in heat flux.

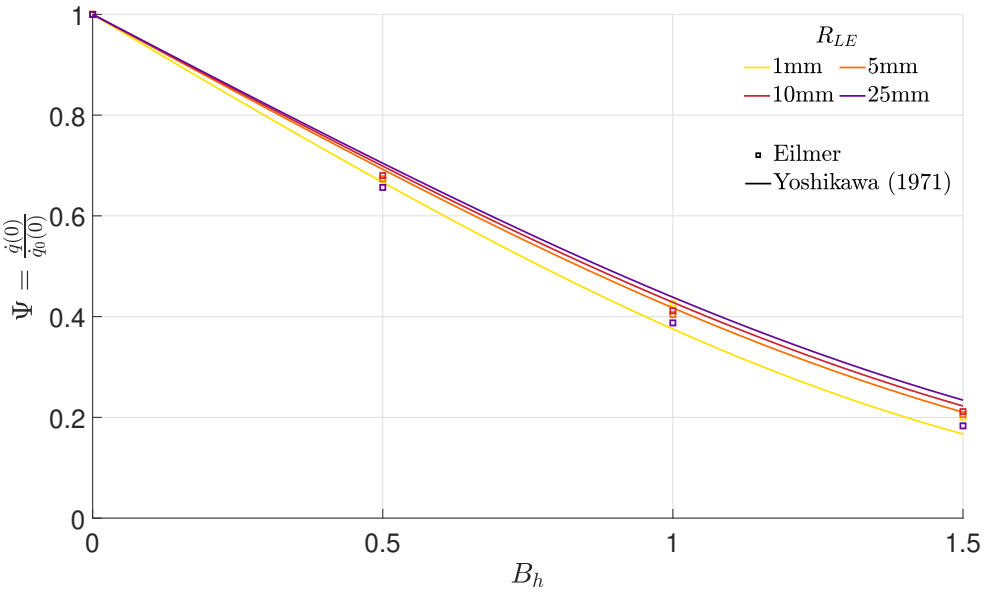


**Figure 19: Stagnation point heat flux numerical results compared to Equation 4.**

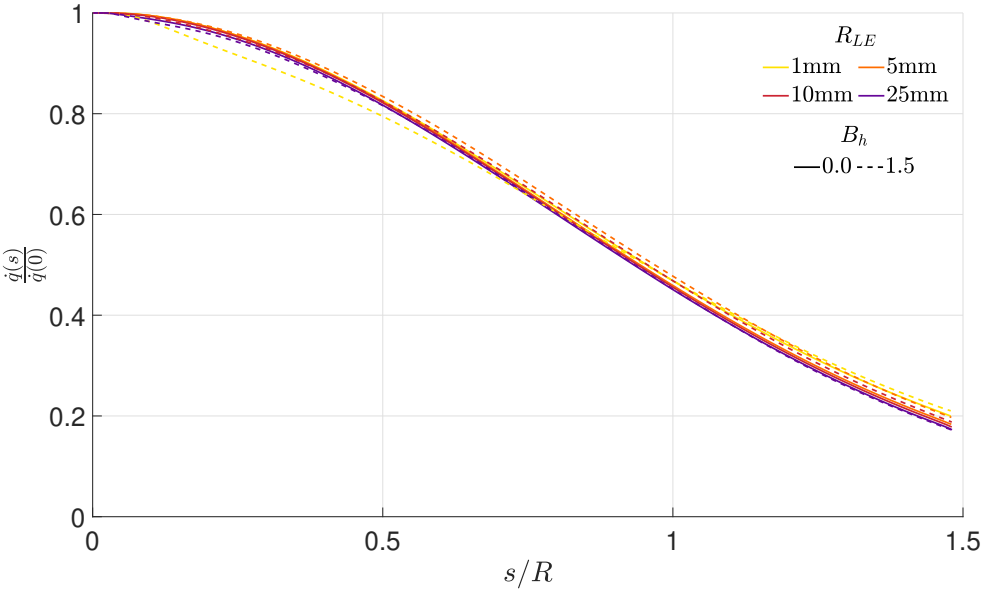


**Figure 20: Normalised heat flux reduction over the porous injector for all radii, and minimum and maximum injection cases.**

### D. Downstream Heat Flux Reduction

The downstream heat flux reduction for both cases are shown in Figure 21. Immediately downstream of the injector, there is an expected decay in heat flux reduction. Far downstream, the heat flux does not return to the nominal uncooled state, but persists at a consistent lower value, the magnitude follows with $B_h$.

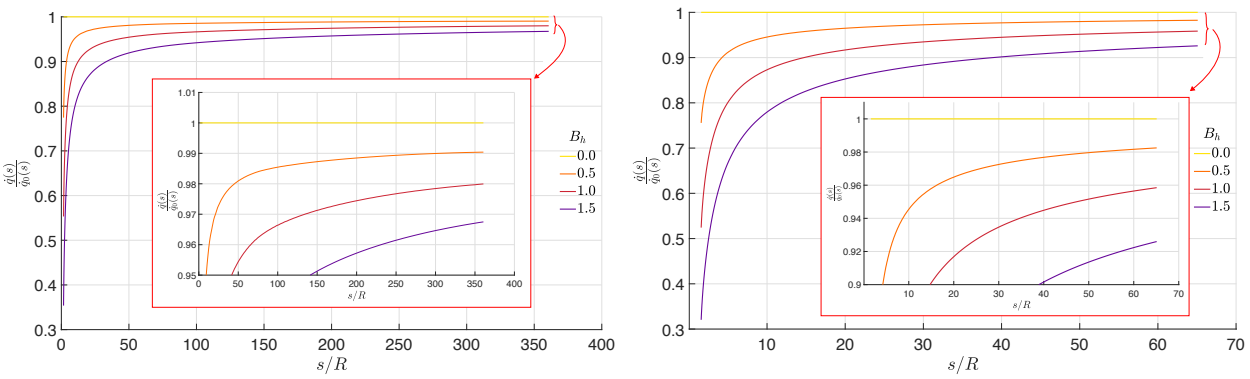


**(a)** $R_{LE}$ **= 1 mm** **(b)** $R_{LE}$ **= 5 mm**

**Figure 21: Downstream heat flux reduction, including a zoomed in regions for the far downstream behaviour.**

Considering the downstream geometry as an inclined flat plate immediately downstream of an injector, the following results will consider the application of the flat plate film cooling correlations described in Section I.

These correlations are adapted and applied to the downstream region to better understand the heat flux reduction both near and far downstream of the porous injection. The flat plate reference coordinates from Figure 2 are adapted for the blunted leading edge injection case, shown in Figure 22.

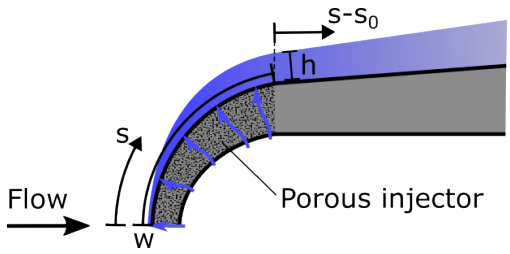


**Figure 22: Blunted leading edge**

The variables in the correlation parameter in Equation 6 were therefore adapted as follows:

- In the case of flat injectors, injected mass flux and therefore $F$ are constant across the injector. For the leading case, an averaged $\bar{F}$ is calculated from local blowing ratio, shown in Equation 21.

$$\bar{F} = \frac{\int_0^{s_0} \rho_c u_c \mathrm{d}s}{\rho_\infty u_\infty} \tag{21}$$

- In [45], $x_{\text{ref}}$ is used to account for the boundary layer state formed along the lead-in length to the slot injector. In this study, $s_{\text{ref}}$ must be adapted to account for the difference in boundary layer state between a blunted leading edge injector, and a downstream injector on a flat plate. An equivalent lead-in length, $s_{\text{ref}}$, is described by the location along a flat plate where the boundary layer edge Reynolds number matches that at the end of the injector, shown in Equation 22. The equivalent flat plate boundary layer was calculated for the same freestream conditions as the leading edge, and the reference length is set using the same power law as in [45]. With these changes, the

correlation parameter is redefined in Equation 23.

$$s_{\text{ref}} = \frac{Re_{\text{inj,end}}\mu_{e,FP}}{\rho_{e,FP}, u_{e,FP}} \tag{22}$$

$$\zeta_{th} = \frac{1}{\bar{F}w}\sqrt{\frac{s - s_0}{s_{\text{ref}}}\frac{C^* s}{Re_u}} \tag{23}$$

This correlation parameter is calculated for the numerical data, and compared to the flat plate correlation in Equation 7, shown in Figure 23. Here, it can be seen that that flat plate correlation predicts a region of overcooling over a short distance immediately downstream of the flat injectors, resulting in $\eta_{th} = 1$. The numerical data in both Figures 21 and 23, shows that this overcooling does not occur anywhere over the injector or downstream of it.

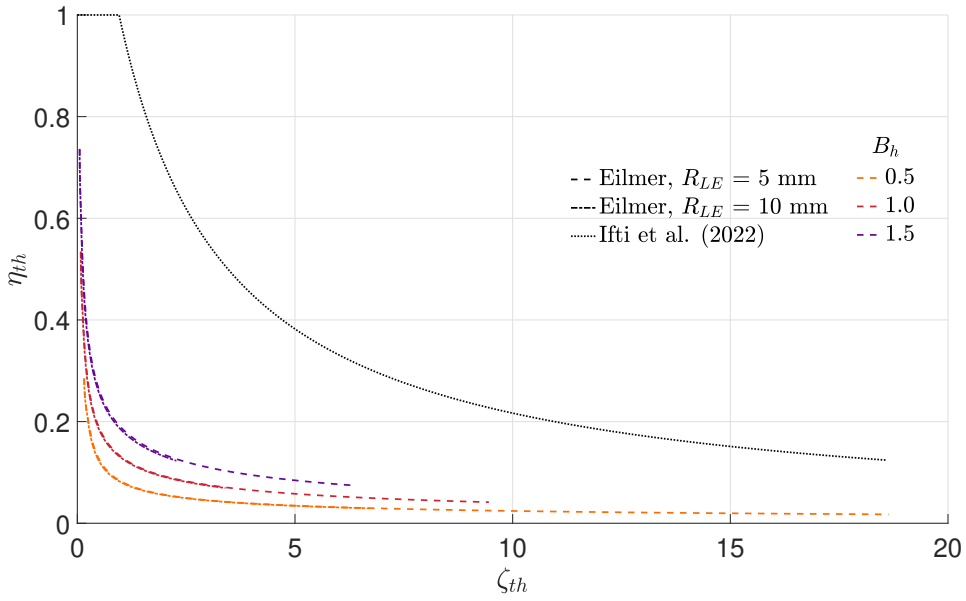


**Figure 23: Film cooling correlation parameter for numerical data for $R_{LE}$ = 5,10 mm; the present work using Equation 24 and a previous flat plate correlation using Equation 7 [44].**

A more meaningful comparison to the flat plate correlation is to compare the thermal efficiency decay rates. Two changes were made to the form of the correlation of $\eta_{th}$ in Equation 7 for application to the leading edge injector simulations:

- To capture the film cooling decay rate, $\eta_{th}$ downstream of the leading edge was normalised by the heat flux reduction at the end of the injector, $\eta_{th}(s_0)$.
- Since the region of overcooling does not occur in these leading edge results, the parameter $\beta$ is removed when adapting Equation 7. However, empirical fitting showed that downstream heat flux (large $\zeta_{th}$) was best captured by adding a constant at the end, $b$.

The reformulated thermal effectiveness correlation applied to the leading edge is shown in Equation 24. The constants were fit against, the $R_{LE}$ = 1 mm case, where constants $a = 5.34$, $b = 0.029$, $c = 0.69$ were found. The updated correlation is shown in Figure 23, and compared against other test cases of $R_{LE}$ = 5, 10 mm. The thermal effectiveness correlation can then be converted back into $s/R$ coordinates to show the downstream cooling distribution in Figure 25.

$$\eta_{th} = \eta_{th}(s_0)[1 + a\zeta_{th}]^c + b \tag{24}$$

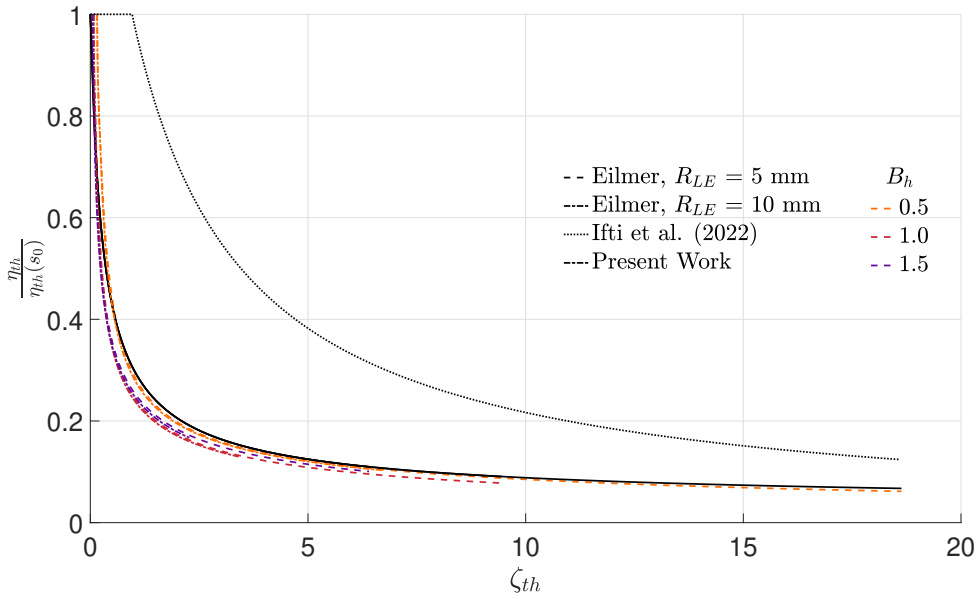


**Figure 24: Normalised film cooling correlation parameter for numerical data for $R_{LE}$ = 5, 10 mm; the present work using Equation 24; and a previous flat plate correlation using Equation 7 [44].**

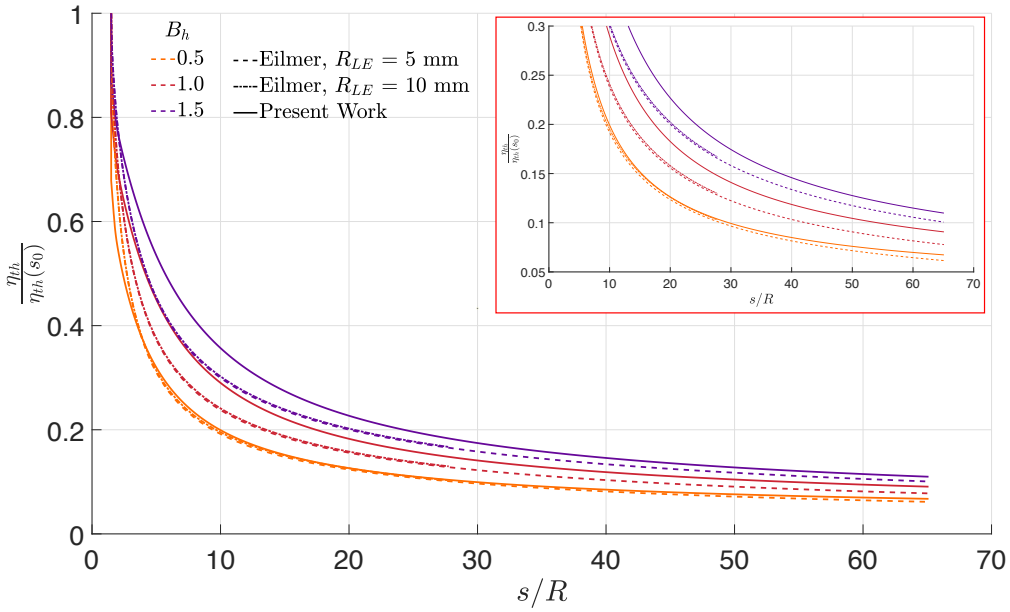


**Figure 25: Normalised film cooling thermal efficiency parameter versus surface coordinate for $R_{LE}$ = 5, 10 mm.**

From Figure 23, the collapsing of the numerical data shows that the modifications made to $\zeta_{th}$ work well for the geometry. However, the correlation parameter does not entirely collapse the thermal effectiveness cases for different $B_h$ values. In Figure 25, the agreement of the new correlation with the data for different $R_{LE}$ cases is good for lower $B_h$ values, but struggles to capture the decay rate of the film cooling for larger $B_h$. The correlation seems to converge back to the numerical data in the far downstream regions.

Further work may seek to improve the empirical correlation coefficients of $\eta_{th}$ using physics-based parameters, especially to capture the thermal effectiveness decay rate. In addition, far downstream behaviour may be more easily compared if the domain is extended for blunter leading edge cases, where the film cooling decay has not yet settled.

### E. Downstream Coolant Concentration

To understand the context of the heat flux reduction shown above, the coolant concentration behaviour was also investigated. Continuing the inclined flat plate analogy, concentration models developed for flat plates may be applied to the downstream region of the body.

In this work, Equation 12 was used to detect the coolant gas slug height distribution along the surface. The flat plate correlation presented in Equation 11, assumes coolant slug convected downstream with velocity $u_e$. For the case of the leading edge, it was found that the boundary layer velocity at the corresponding slug height led to a better correlation fit. Profiles of the concentration and velocity within the boundary layer at streamwise locations are shown in Figure 26. Detected slug height is also shown, and it can be seen that estimated slug velocity increases as a fraction of $u_e$ as the slug is convected downstream. The modified correlation parameter is shown in Equation 25.

$$\zeta_c = \sqrt{\frac{u_h h^2}{4D_{12}(x - x_0)}} \tag{25}$$

Using this modified parameter, it was found that the correlation of Equation 11 did not fully capture the concentration decay after the downstream injector. The correlation parameter was fit against $\eta_c$ for the $R_{LE}$ = 1 mm case. An updated correlation is provided below in Equation 26, where $a$ = 1.69, $b$ = 0.206, and $c$ = 5.07. The updated correlation is shown in Figure 27, and is once more compared against the $R_{LE}$ = 5, 10 mm cases. The comparison is then converted back into the original surface coordinates, and shown in Figure 28.

$$\eta_c = \eta_c(s_0)\left(\mathrm{erf}(a\zeta_c^b)\right)^c \tag{26}$$

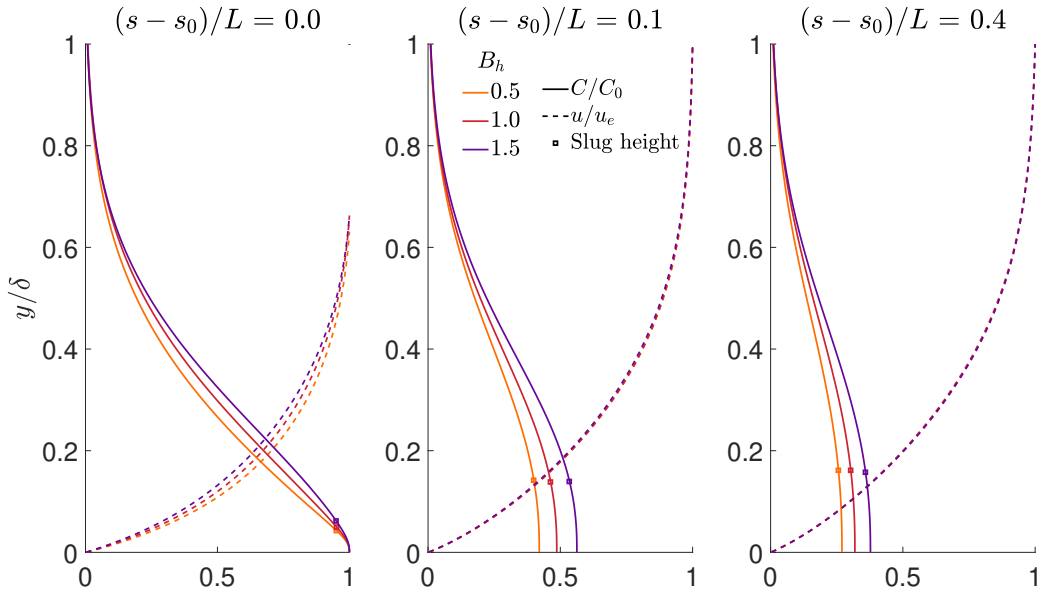


**Figure 26: Concentration and velocity profiles within the boundary layer, showing the concentration-based coolant slug height, and the corresponding slug velocity.**

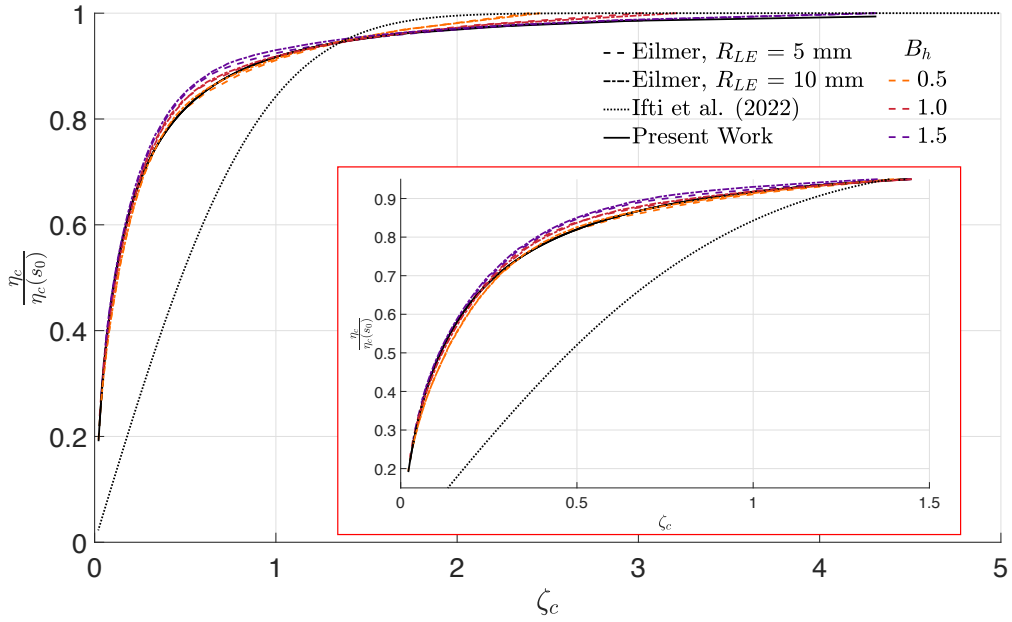


**Figure 27: Concentration parameter versus film concentration efficiency for cases $R_{LE}$ = 1,5 mm, including the original model [49], and the model used in the current work.**

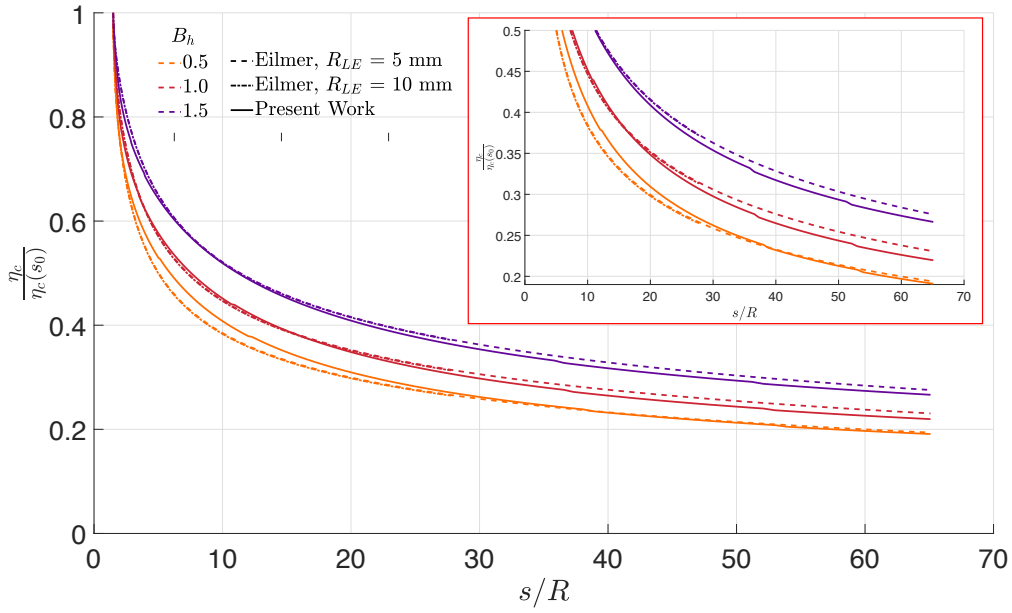


**Figure 28: Film cooling concentration efficiency parameter versus surface coordinate for $R_{LE}$ = 1,5 mm.**

Similar to the thermal effectiveness, the concentration effectiveness correlation parameter works well, but does not perfectly collapse all the $B_h$ cases together, but does do so for the different $R_{LE}$, as shown in Figure 27. Further work is required to find a correlation parameter that would collapse these curves onto a single line. The decay rate of the concentration is reasonably matched close to the injector. Further modelling work is required to adapt the $\eta_c$ correlation coefficients to incorporate a physical grounding for the far downstream concentrations, as seen in Figure 28. The overall correlation, when compared to the original flat plate correlation function, matches the numerical data much better, possibly due to the assumption of the velocity of the coolant slab.

# IV. Conclusion

Numerical simulations were carried out on a hypersonic sharp leading edge with distributed leading edge transpiration cooling at a flight condition, to understand the trade-off between drag and heat flux due to moderate blowing parameters and varying radii. The results showed that mass injection had very little affect on the body drag, but significantly reduced heat flux at the stagnation point and over the leading edge, indicating that transpiration cooling enables the survivability of sharper leading edges for sustained hypersonic flight.

The leading edge heat flux could be collapsed across radii and blowing parameters. The effects of mass injection were shown to persist far downstream in the form of heat flux reduction, boundary layer thickness and shock layer thickness. Empirical modifications to existing film cooling correlations to predict thermal and concentration effectiveness were made, and shown to reasonably predict the downstream cooling behaviour. Further work may explore grounding these modifications in the flow physics to produce an overall model for such transpiration-cooled geometries. Other additional work could examine the effect of large blowing parameters on the drag, or the effect of different freestream conditions and coolants on the coolant correlations.

# Appendix

## A. Pressure and Skin Friction Distributions

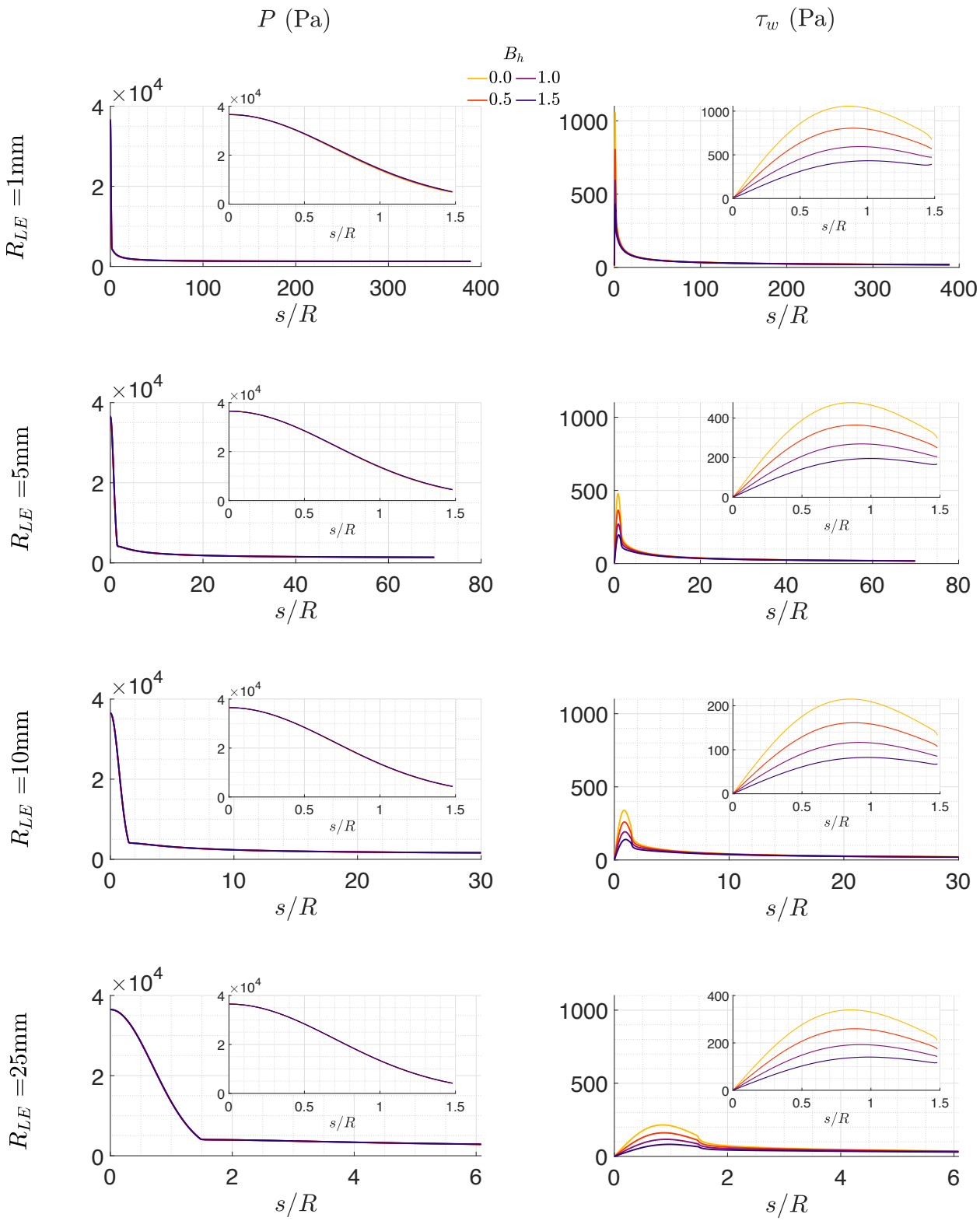


**Figure 29: Force distributions acting on the whole body, and also zoomed into the leading edge porous injector for each radius and blowing parameter.**

## Acknowledgments

The authors would like to acknowledge the use of the University of Oxford Advanced Research Computing (ARC) facility [71] in carrying out this work.

## References

[1] Reuther, J., Kinney, D., Smith, S., Kontinos, D., Gage, P., and Saunders, D., *A reusable space vehicle design study exploring sharp leading edges*, 35th AIAA Thermophysics Conference, American Institute of Aeronautics and Astronautics, 2001. https://doi.org/10.2514/6.2001-2884.

[2] Ohlhorst, C. W., Glass, D. E., Bruce, W. E., Lindell, M. C., Vaughn, W. L., Smith, R. W., Dirling, R. B., Hogenson, P. A., Nichols, J. M., Risner, N. W., Thompson, D. R., Kowbel, W., Sullivan, B. J., Koenig, J. R., and Cuneo, J. C., *Development of X-43A Mach 10 Leading Edges*, 56th International Astronautical Congress of the International Astronautical Federation, the International Academy of Astronautics, and the International Institute of Space Law, American Institute of Aeronautics and Astronautics, 2005. https://doi.org/10.2514/6.IAC-05-D2.5.06, 09; M1: 0; doi:10.2514/6.IAC-05-D2.5.06.

[3] Kelly, H. N., and Blosser, M. L., "Active cooling from the sixties to NASP," Tech. rep., National Aeronautics and Space Administration., October 1st 1992. Report No. NASA-N93-12458.

[4] Chen, X.-q., Hou, Z.-x., Liu, J.-x., and Gao, X.-z., "Bluntness impact on performance of waverider," *Computers and Fluids*, Vol. 48, No. 1, 2011, pp. 30–43. https://doi.org/10.1016/j.compfluid.2011.03.011.

[5] Liu, J.-x., Hou, Z.-x., Ding, G.-h., Chen, X.-q., and Chen, X.-q., "Numerical and experimental study on waverider with blunt leading edge," *Computers and Fluids*, Vol. 84, 2013, pp. 203–217. https://doi.org/10.1016/j.compfluid.2013.06.005.

[6] Santos, W. F. N., "Bluntness Impact on Lift-to-Drag Ratio of Hypersonic Wedge Flow," *Journal of Spacecraft and Rockets*, Vol. 46, No. 2, 2009, pp. 329–339. https://doi.org/10.2514/1.41387.

[7] Sutton, K., and Graves, R. A., "A general stagnation-point convective heating equation for arbitrary gas mixtures," Tech. rep., National Aeronautics and Space Administration, 1971. Report No. NASA-TR-R-376.

[8] Böhrk, H., Dittert, C., Weihs, H., Thiele, T., and Gülhan, A., "Sharp Leading Edge at Hypersonic Flight: Modeling and Flight Measurement," *Journal of Spacecraft and Rockets*, Vol. 51, No. 5, 2014, pp. 1753–1760. https://doi.org/10.2514/1.A32892.

[9] Gülhan, A., and Braun, S., "An experimental study on the efficiency of transpiration cooling in laminar and turbulent hypersonic flows," *Experiments in fluids*, Vol. 50, No. 3, 2010, pp. 509–525. https://doi.org/10.1007/s00348-010-0945-6.

[10] Steeves, C. A., He, M. Y., Kasen, S. D., Valdevit, L., Wadley, H. N. G., and Evans, A. G., "Feasibility of Metallic Structural Heat Pipes as Sharp Leading Edges for Hypersonic Vehicles," *Journal of Applied Mechanics*, Vol. 76, No. 3, 2009. https://doi.org/10.1115/1.3086440.

[11] Hermann, T. A., McGilvray, M., Ifti, H. S., Hufgard, F., and Loehle, S., "Fluid-Solid Heat Exchange in Porous Media for Transpiration Cooling Systems," American Institute of Aeronautics and Astronautics, San Diego, California, 2019. https://doi.org/10.2514/6.2019-0537.

[12] Ifti, H. S., Hermann, T., Ewenz Rocher, M., Doherty, L., Hambidge, C., McGilvray, M., and Vandeperre, L., "Laminar transpiration cooling experiments in hypersonic flow," *Experiments in Fluids*, Vol. 63, No. 6, 2022, p. 102. https://doi.org/10.1007/s00348-022-03446-1.

[13] Rocher, M. E., McGilvray, M., Hermann, T. A., Ifti, H. S., Hufgard, F., Eberhart, M. F., Meindl, A., Loehle, S., Giovannini, T., and Vandeperre, L. J., "Testing a Transpiration Cooled Zirconium-Di-Boride sample in the Plasma Tunnel at IRS," American Institute of Aeronautics and Astronautics, San Diego, California, 2019. https://doi.org/10.2514/6.2019-1552.

[14] Chauvin, L. T., and Carter, H. S., "Exploratory tests of transpiration cooling on a porous 8 degree cone at M=2.05 using nitrogen gas, helium gas and water as the coolants," Tech. rep., National Advisory Committee for Aeronautics, 1955. Report No. NACA-RM-L55C29.

[15] Rubesin, M. W., "An Analytical Estimation of the Effect of Transpiration Cooling on the Heat-Transfer and Skin-Friction Characteristics of a Compressible, Turbulent Boundary Layer," Tech. rep., National Advisory Committee for Aeronautics, 1954. Report No. NACA-TN-3341.

[16] Schneider, P. J., Maurer, R. E., and Strapp, M. G., "Two-dimensional transpiration-cooled nosetip," *Journal of Spacecraft and Rockets*, Vol. 8, No. 2, 1971, pp. 170–176. https://doi.org/10.2514/3.30239.

[17] Campbell, N. C., Pittinato, G. F., and Martin, M. T., "Transpiration Cooled Nosetip Development," Tech. rep., Army Materials and Mechanics Research Center, 1980. Report No. DAA G46-78-C-0034.

[18] Yoshikawa, K. K., "Linearized theory of stagnation point heat and mass transfer at hypersonic speeds," Tech. rep., NASA Ames Research Centre, 1971. Report No. NASA-TN-D-6262.

[19] Cresci, R. J., "Theoretical analysis of the downstream influence of mass transfer in a stagnation region," *International Journal of Heat and Mass Transfer*, Vol. 5, No. 9, 1962, pp. 837–857. https://doi.org/10.1016/0017-9310(62)90183-7.

[20] LIBBY, P. A., and CRESCI, R. J., "Experimental Investigation of the Downstream Influence of Stagnation-Point Mass Transfer," *Journal of the Aerospace Sciences*, Vol. 28, No. 1, 1961, pp. 51–64. https://doi.org/10.2514/8.8852.

[21] Gollnick, A. F., "An experimental study of thermal diffusion effects on a partially porous mass transfer-cooled hemisphere," *International Journal of Heat and Mass Transfer*, Vol. 7, No. 7, 1964, pp. 699–708. https://doi.org/10.1016/0017-9310(64)90001-8.

[22] Kaattari, G., "Effects of mass addition on blunt-body boundary-layer transition and heat transfer," Tech. rep., National Aeronautics and Space Administration, 1978. Report No. NASA-TP-1139.

[23] Cresci, R. J., and Libby, P. A., "The Downstream Influence of Mass Transfer at the Nose of a Slender Cone," *Journal of the Aerospace Sciences*, Vol. 29, No. 7, 1962, pp. 815–826. https://doi.org/10.2514/8.9610.

[24] Pappas, C. C., and Lee, G., "Heat transfer and pressure on a hypersonic blunt cone with mass addition," *AIAA Journal*, Vol. 8, No. 5, 1970, pp. 954–956. https://doi.org/10.2514/3.5801.

[25] Lewis, C. H., Adams, J. C., and Gilley, G. E., "Effects of Mass Transfer and Chemical Nonequilibrium on Slender Blunted Cone Pressure and Pressure and Heat-Transfer Distributions at M = 13.2," Tech. rep., Arnold Engineering Development Center, 1968. Report No. AEDC-TR-68-214.

[26] Pappas, C. C., and Okuno, A. F., "The relation between skin friction and heat transfer for the compressible turbulent boundary layer with gas injection," Tech. rep., National Aeronautics and Space Administration, 1965. Report No. NASA-TN-D-2857.

[27] Dunavant, J. C., and Everhart, P. E., "Explorator heat-transfer measurements at Mach 10 on a 7.5 deg total-angle cone downstream of a region of air and helium transpiration cooling," Tech. rep., National Aeronautics and Space Administration, 1969. Report No. NASA-TN-D-5554.

[28] Böhrk, H., Wartemann, V., Eggers, T., Martinez Schramm, J., Wagner, A., and Hannemann, K., "Shock Tube Testing of the Transpiration-Cooled Heat Shield Experiment AKTiV," American Institute of Aeronautics and Astronautics, 2012. https://doi.org/10.2514/6.2012-5935.

[29] Kuhn, M., and Hald, H., "Application of Transpiration Cooling for Hot Structures," Springer Berlin Heidelberg, Berlin, Heidelberg, 2008, pp. 82–103. https://doi.org/10.1007/978-3-540-77819-6_6.

[30] Ewenz-Rocher, M., Hermann, T., McGilvray, M., Quinn, M., and Ifti, H., "Studying the film effectiveness of transpiration cooled walls using pressure sensitive paint," European Space Agency, Monopoli, Italy, 2019.

[31] Naved, I., Hermann, T., McGilvray, M., Ewenz Rocher, M., Hambidge, C., Doherty, L., Le Page, L., Grossman, M., and Vandeperre, L., "Heat Transfer Measurements of a Transpiration-Cooled Stagnation Point in Transient Hypersonic Flow," *Journal of Thermophysics and Heat Transfer*, 2022. https://doi.org/10.2514/1.T6610.

[32] Ding, R., Wang, J., He, F., Dong, G., and Tang, L., "Numerical investigation on the performances of porous matrix with transpiration and film cooling," *Applied Thermal Engineering*, Vol. 146, 2019, pp. 422–431. https://doi.org/10.1016/j.applthermaleng.2018.09.134.

[33] Dittert, C., Selzer, M., and Böhrk, H., "Flowfield and Pressure Decay Analysis of Porous Cones," *AIAA Journal*, Vol. 55, No. 3, 2017, pp. 874–882. https://doi.org/10.2514/1.J055298.

[34] Kerth, P., Wylie, S., Ravichandran, R., and McGilvray, M., "Gas Injection into Second Mode Instability on a 7 degree Cone at Mach 7," *AIAA AVIATION 2022 Forum*, American Institute of Aeronautics and Astronautics, Chicago, IL, USA, 2022. https://doi.org/10.2514/6.2022-3856.

[35] Jiang, P.-X., Huang, G., Zhu, Y., Liao, Z., and Huang, Z., "Experimental investigation of combined transpiration and film cooling for sintered metal porous struts," *International Journal of Heat and Mass Transfer*, Vol. 108, 2017, pp. 232–243. https://doi.org/10.1016/j.ijheatmasstransfer.2016.12.014.

[36] Ding, R., Wang, J., He, F., Wang, M., Luan, Y., Dong, G., and Tang, L., "Numerical investigation on a double layer combined cooling structure for aerodynamic heat control of hypersonic vehicle leading edge," *Applied Thermal Engineering*, Vol. 169, 2020. https://doi.org/10.1016/j.applthermaleng.2020.114949.

[37] Luo, S., Miao, Z., Liu, J., Song, J., Xi, W., and Liu, C., "Effects of Coolants of Double Layer Transpiration Cooling System in the Leading Edge of a Hypersonic Vehicle," *Frontiers in Energy Research*, Vol. 9, 2021. https://doi.org/10.3389/fenrg.2021.756820.

[38] Wu, N., Wang, J., He, F., Chen, L., and Ai, B., "Optimization transpiration cooling of nose cone with non-uniform permeability," *International Journal of Heat and Mass Transfer*, Vol. 127, 2018, pp. 882–891. https://doi.org/10.1016/j.ijheatmasstransfer.2018.07.134.

[39] Brune, A., Hosder, S., Gulli, S., and Maddalena, L., "Variable Transpiration Cooling Effectiveness in Laminar and Turbulent Flows for Hypersonic Vehicles," *AIAA Journal*, Vol. 53, No. 1, 2015, pp. 176–189. https://doi.org/10.2514/1.J053053.

[40] Gulli, S., Maddalena, L., Brune, A., and Hosder, S., "Integrated Analysis of Reusable Thermal Protection Systems Based on Variable-Transpiration Cooling," *Journal of Spacecraft and Rockets*, Vol. 51, No. 2, 2014, pp. 412–423. https://doi.org/10.2514/1.A32692.

[41] Connolly, J., *Geometry Dependence of Transpiration Cooling for Hypersonic Systems*, AIAA Scitech 2021 Forum, American Institute of Aeronautics and Astronautics, 2021. https://doi.org/10.2514/6.2021-1519.

[42] Swann, R. T., and Pittman, C. M., "Numerical Analysis of the Transient Response of Advanced Thermal Protection Systems for Atmospheric Entry," Tech. rep., National Aeronautics and Space Administration, 1962. Report No. NASA-TN-D-1370.

[43] Naved, I., Hermann, T., Hambidge, C., Saad Ifti, H., Falsetti, C., McGilvray, M., Tirichenko, I. S., and Vandeperre, L., "Transpiration-Cooling Heat Transfer Experiments in Laminar and Turbulent Hypersonic Flows," *Journal of Thermophysics and Heat Transfer*, 2022. https://doi.org/10.2514/1.T6626.

[44] Ifti, H. S., Hermann, T., McGilvray, M., and Merrifield, J., "Numerical Simulation of Transpiration Cooling in a Laminar Hypersonic Boundary Layer," *Journal of Spacecraft and Rockets*, Vol. 59, No. 5, 2022, pp. 1726–1735. https://doi.org/10.2514/1.A35325.

[45] Heufer, K. A., and Olivier, H., "Experimental and Numerical Study of Cooling Gas Injection in Laminar Supersonic Flow," *AIAA Journal*, Vol. 46, No. 11, 2008, pp. 2741–2751. https://doi.org/10.2514/1.34218.

[46] Hombsch, M., and Olivier, H., "Film Cooling in Laminar and Turbulent Supersonic Flows," *Journal of Spacecraft and Rockets*, Vol. 50, No. 4, 2013, pp. 742–753. https://doi.org/10.2514/1.A32346.

[47] Martelli, E., Nasuti, F., and Onofri, M., "Numerical Analysis of Film Cooling in Advanced Rocket Nozzles," *AIAA Journal*, Vol. 47, No. 11, 2009, pp. 2558–2566. https://doi.org/10.2514/1.39217.

[48] Eckert, E. R., "Survey on Heat Transfer at High Speeds," Tech. rep., Armed Services Technical Information Agency, Dec 1961.

[49] Ifti, H. S., "Transpiration Cooling of a Hypersonic Vehicle," Ph.D. thesis, Feb 14, 2022.

[50] Bird, R. B., Stewart, W. E., and Lightfoot, E. N., *Appendix E. Tables for Prediction of Transport Properties.*, revised 2nd edition ed., Transport Phenomena, Wiley, New York, 1960.

[51] Gibbons, N. N., Damm, K. A., Jacobs, P. A., and Gollan, R. J., "Eilmer: an Open-Source Multi-Physics Hypersonic Flow Solver," *Computer Physics Communications*, Vol. 282, 2023, p. 108551. https://doi.org/https://doi.org/10.1016/j.cpc.2022.108551.

[52] Jacobs, P. J., Gollan, R. J., Damm, K. A., and Gibbons, N. N., "GDTk: The Gas Dynamics Toolkit," , 2022. URL https://gdtk.uqcloud.net/, accessed: 2022-11-28.

[53] Jacobs, P., Gollan, R., Denman, A., O'Flaherty, B., Potter, D., Petrie-Repar, P., and Johnston, I., "Eilmer's theory book: Basic models for gas dynamics and thermochemistry," Mechanical engineering report 2010/09, The University of Queensland, 2012.

[54] Jacobs, P., and Gollan, R., "Implementation of a compressible-flow simulation code in the D programming language," *Applied Mechanics and Materials*, Vol. 846, Trans Tech Publ, 2016, pp. 54–60. https://doi.org/10.4028/www.scientific.net/AMM.846.54.

[55] Gollan, R., and Jacobs, P., "About the formulation, verification and validation of the hypersonic flow solver Eilmer," *International Journal for Numerical Methods in Fluids*, Vol. 73, No. 1, 2013, pp. 19–57. https://doi.org/10.1002/fld.3790.

[56] Lees, L., "Laminar Heat Transfer Over Blunt-Nosed Bodies at Hypersonic Flight Speeds," *Journal of Jet Propulsion*, Vol. 26, No. 4, 1956, pp. 259–269. https://doi.org/10.2514/8.6977.

[57] Hermann, T., McGilvray, M., and Naved, I., "Performance of Transpiration-Cooled Heat Shields for Reentry Vehicles," *AIAA Journal*, Vol. 58, No. 2, 2020, pp. 830–841. https://doi.org/10.2514/1.J058515.

[58] Ewenz Rocher, M., Hermann, T., McGilvray, M., and Gollan, R., "Correlation for Species Concentration on a Hypersonic Stagnation Point with Mass Injection," *AIAA journal*, Vol. 60, No. 5, 2022, pp. 2798–2809. https://doi.org/10.2514/1.J061159.

[59] Gupta, R. N., Yos, J. M., Thompson, R. A., and Lee, K.-P., "A review of reaction rates and thermodynamic and transport properties for an 11-species air model for chemical and thermal nonequilibrium calculations to 30000 K," *NASA Reference Publication 1232*, 1990.

[60] McBride, B. J., Zehe, M. J., and Gordon, S., "NASA Glenn coefficients for calculating thermodynamic properties of individual species," Tech report 211556, National Aeronautics and Space Administration, 2002.

[61] Wilke, C., "A viscosity equation for gas mixtures," *The journal of chemical physics*, Vol. 18, No. 4, 1950, pp. 517–519.

[62] Gordon, S., and McBride, B. J., "Computer program for calculation of complex chemical equilibrium compositions and applications. Part 1: Analysis," *NASA Reference Publication 1311*, 1994.

[63] Wada, Y., and Liou, M.-S., "A flux splitting scheme with high-resolution and robustness for discontinuities," *32nd Aerospace Sciences Meeting and Exhibit*, Reno, Nevada, 1994, pp. AIAA paper 1994–83. https://doi.org/https://doi.org/10.2514/6.1994-83.

[64] Wada, Y., and Liou, M.-S., "An accurate and robust flux splitting scheme for shock and contact discontinuities," *SIAM Journal on Scientific Computing*, Vol. 18, No. 3, 1997, pp. 633–657. https://doi.org/10.1137/S1064827595287626.

[65] Van Albada, G. D., Leer, B. v., and Roberts, W., "A comparative study of computational methods in cosmic gas dynamics," *Upwind and high-resolution schemes*, Springer, 1997, pp. 95–103. https://doi.org/10.1007/978-3-642-60543-7_6.

[66] Drayna, T. W., "Design and Optimization of Hypersonic Inward-Turning Inlets," Ph.D. thesis, University of Minnesota, 2011.

[67] Haselbacher, A., and Blazek, J., "On the accurate and efficient discretisation of the Navier-Stokes equations on mixed grids," *14th Computational Fluid Dynamics Conference*, Norfolk, Virginia, 1999, pp. 946–956. https://doi.org/10.2514/6.1999-3363.

[68] Damm, K. A., "Adjoint-Based Aerodynamic Design Optimisation in Hypersonic Flow," Ph.D. thesis, University of Queensland, 2020. https://doi.org/https://doi.org/10.14264/uql.2020.207.

[69] Saad, Y., *Iterative methods for sparse linear systems*, Vol. 82, siam, 2003.

[70] Mangler, W., "Zusammenhang zwischen ebenen und rotationssymmetrischen Grenzschichten in kompressiblen Flüssigkeiten," *ZAMM-Journal of Applied Mathematics and Mechanics/Zeitschrift für Angewandte Mathematik und Mechanik*, Vol. 28, No. 4, 1948, pp. 97–103.

[71] Richards, A., *University of Oxford Advanced Research Computing*, Aug. 2015. https://doi.org/10.5281/zenodo.22558.